By acceptance of this article, the publisher or recipient acknowledges the U.S. Government's right to retain a nonexclusive, royalty-free license in and to any copyright covering the article.

MASTER

CONF-790839--2

QUANTITATIVE X-RAY MICROANALYSIS IN AN AEM: INSTRUMENTAL CONSIDERATIONS AND APPLICATIONS TO MATERIALS SCIENCE

by

Nestor J. Zaluzec
Metals and Ceramics Division
Oak Ridge National Laboratory
Radiation Effects and Microstructural Analysis Group

NOTICE
This report was prepared as an account of work sponsored by the United States Government. Neither the United States nor the United States Department of Energy, nor any of their employees, nor any of their contractors, subcontractors, or their employees, makes any warranty, express or implied, or assumes any legal liability or responsibility for the accuracy, completeness or usefulness of any information, apparatus, product or process disclosed, or represents that its use would not infringe privately owned rights.

To be published as a chapter in: Analytical Electron Microscopy
ed. Hren, Joy, Goldstein; pub. Plenum Press (Fall, 1979
sponsored jointly by EMSA and MAS

DISTRIBUTION OF THIS DOCUMENT IS UNLIMITED

CHAPTER 4

QUANTITATIVE X-RAY MICROANALYSIS: INSTRUMENTAL CONSIDERATIONS AND APPLICATIONS TO MATERIALS SCIENCE

NESTOR J. ZALUZEC
METALS AND CERAMICS DIVISION, OAK RIDGE NATIONAL LABORATORY
RADIATION EFFECTS AND MICROSTRUCTURAL ANALYSIS GROUP
OAK RIDGE, TENNESSEE 37830

4.1 INTRODUCTION

4.2 INSTURMENTAL LIMITATIONS IN AEM BASED X-RAY MICROANALYSIS

4.3 INSTRUMENTAL ARTIFACTS: SYSTEMS BACKGROUND

Fluorescence by Uncollimated Radiation: Remote Sources

Fluorescence by Uncollimated Radiation: Local Sources

Detector Artifacts

4.4 OPTIMUM EXPERIMENTAL CONDITIONS FOR X-RAY ANALYSIS

Detector/Specimen Geometry

Detector Collimation

Selection of Incident Beam Energy and Electron Source

Imaging and Diffraction Conditions During Analysis

Specimen Preparation Artifacts

4.5 DATA REDUCTION FOR QUANTITATIVE ANALYSIS

4.5 APPLICATION OF QUANTITATIVE X-RAY MICROANALYSIS:

Parameters of Standardless Analysis

Absorption Correction

4.6 APPLICATIONS OF STANDARDLESS ANALYSIS

Standardless Analysis Using the Thin-Film Approximation: Fe-13r-40Ni

Standardless Analysis Using the Absorption Correction: β NiAl

4.7 STANDARDLESS ANALYSIS IN COMPLEX SYSTEMS

Analysis of Totally Buried Peaks

Quantitative Analysis of Precipitate Phases

Procedures for Analysis of Radioactive Specimens

SUMMARY

ACKNOWLEDGMENTS

CHAPTER 4

QUANTITATIVE X-RAY MICROANALYSIS: INSTRUMENTAL CONSIDERATIONS AND APPLICATIONS TO MATERIALS SCIENCE

NESTOR J. ZALUZEC
METALS AND CERAMICS DIVISION, OAK RIDGE NATIONAL LABORATORY
RADIATION EFFECTS AND MICROSTRUCTURAL ANALYSIS GROUP
OAK RIDGE, TENNESSEE 37830

4.1 INTRODUCTION

X-ray microanalysis using a modern transmission or scanning transmission electron microscope (TEM/STEM) is an extremely powerful analytical tool. The ability to observe and characterize the morphology, crystallography, and elemental composition of regions of a specimen as small as 20 nm in diameter is a major breakthrough for materials science. In this chapter the practical aspects of the application of x-ray microanalysis to nonbiological systems will be considered (the use of this technique in biological research is the topic of Chapter 5). This chapter will first deal with optimizing the instrumental factors which influence microanalysis, namely: the specimen/detector geometry; the choice of accelerating voltage, electron gun, imaging mode, and most importantly the elimination of instrumental artifacts. The application of the principles of thin film analysis to simple single phase samples will then be considered, followed by a discussion of multiphase systems where analysis and interpretation becomes more complex. These examples will be drawn primarily from the author's own experience, because of the difficulties inherent to reconstructing complete experimental details from the literature. The published applications of several other authors are cited in the bibliography.

4.2 INSTURMENTAL LIMITATIONS IN AEM BASED X-RAY MICROANALYSIS

The general principles of thin film x-ray microanalysis in an analytical electron microscope (AEM) have been outlined in Chapter 3. Before applying the techniques described there to quantitative analysis, it is important to consider the instrumental factors which influence the information recorded by the x-ray detector system. Thus, this section will first consider the problems associated with the interfacing of a solid state energy dispersive x-ray spectrometer (EDS) to the column of an electron microscope, and then concentrate on optimizing the AEM

system to minimize spectral artifacts. For the most part, the limitations in TEM/STEM based microanalysis are purely instrumental and can be corrected through judicious modification of the electron-optical column. Complications arise because the present generation of analytical electron microscopes have evolved from the addition of analytical attachments to TEM or STEM instruments rather than being designed from the outset as true AEMs.

4.3 INSTRUMENTAL ARTIFACTS: SYSTEMS BACKGROUND

Ideally, the measured x-ray spectrum should be due solely to the interaction of the incident electron probe with the microvolume of material it irradiates. Unfortunately, in the majority of instruments in use today this is not the case, although it is now being corrected by the manufacturers in the new instruments. The phenomenon is most easily observed by allowing the incident probe to pass through a small hole in a suitable specimen. In such a situation one would expect all characteristic emission to cease. This is usually the exception rather than the rule. Remotely produced uncollimated radiation (electrons and/or x-rays) from the electron-optical column continuously bombards the sample and its immediate surroundings independent of the electron probe position. This radiation can induce fluorescence of the specimen and its environment thereby producing additional x-ray emission. The nature, strength and source of this uncollimated radiation varies from instrument to instrument; however, the result is the same - degradation of the high spatial resolution and the accuracy of the obtained quantitative information. Clearly, the reduction or elimination of this radiation in an AEM is an important aspect of x-ray microanalysis. It has been the subject of much study during the last few years: (GEISS and HUANG, 1975; ZALUZEC and FRASER, 1976, 1977, 1978; JOY and MAHER, 1976; SHUMAN et al., 1976; HREN et al., 1976; GOLDSTEIN and WILLIAMS, 1977; MORRIS et al., 1977; NICHOLSON et al., 1977; ZALUZEC et al., 1978; HEADLEY and HREN, 1978) as well as a recent comprehensive tutorial (BENTLEY et al., 1979) from which this discussion draws heavily. In addition to fluorescence of the specimen, x-rays characteristic of the support grids, goniometer stage, anti-contamination devices, pole pieces, and any other materials in the immediate vicinity of the sample are frequently detected. These x-rays are a result of fluorescence by the remotely produced uncollimated radiation as well as by locally scattered electrons and/or x-rays produced by the interaction of the focussed electron probe with the specimen. All of this nonlocalized fluorescence of the specimen and its environment can be classified as "systems background" (JOY and MAHER, 1976).* The discussion which follows will be loosely divided into two parts (with some overlap): (1) background resulting from remote sources of uncollimated fluorescing radiation, and (2) that resulting from sources local to the specimen.

*Systems background is used in its most general sense to include all measured characteristic or continuum x-rays which do not result directly from the excitation of the specimen by the focussed electron probe. The term spurious x-rays used in Chapter 3 is roughly equivalent.

Fluorescence by Uncollimated Radiation: Remote Sources

In order to produce the fine electron probes used in an AEM it is usually necessary to intercept a relatively large electron flux by a series of beam defining apertures. These apertures can act as excellent sources of uncollimated radiation: electrons (not confined to the incident probe) and x-rays (both characteristic and continuum).

Depending on the specific design of the condensor aperture system, it is possible for electrons to scatter around the periphery of the fixed and variable aperture support mechanisms. These electrons, together with any that are scattered from the bore of contaminated or thick apertures, can result in the formation of significant electron tails (i.e., electrons not confined to the immediate diameter of the focussed probe) and thus can produce characteristic x-rays from regions of the specimen outside the primary electron probe. A second type of uncollimated radiation can also be traced directly to the various beam defining apertures. Typical condensor apertures are relatively thin, high atomic number materials of sufficient mass thickness to completely stop the incident electrons but substantially transparent to hard x-rays. Conditions such as this are nearly perfect for these apertures to act as thin target x-ray sources (both characteristic and Bremmstrahlung). The situation is further aggrevated by the fact that the emission of Bremmstrahlung is highly anistotropic. At the electron energies typical of AEM investigations ($\geq$ 100 keV) this emission is peaked in the forward scattering direction. Thus, in an AEM one can find the conditions and geometry nearly ideal for x-ray fluorescence of the specimen and its environment. Fig. 4.1a schematically illustrates these remote sources.

Figure 4.1. (a) Schematic illustration of remote sources of uncollimated fluorescing radiation from fixed (A) and variable(B) beam defining apertures. (b) Minimization techniques using thick fixed apertures (A) above the variable beam defining aperture (B), thick spray apertures (C) below the C_2 aperture, and non-beam defining apertures (D) just above the objective lens pole piece.

The choice of the test specimen used to assess the prescence and nature of the uncollimated radiation is critical. One of the best is of the self-supporting, thinned disc variety. The periphery of the specimen is effectively a thick ($\geq$ 0.1 mm) rim of material representing a bulk

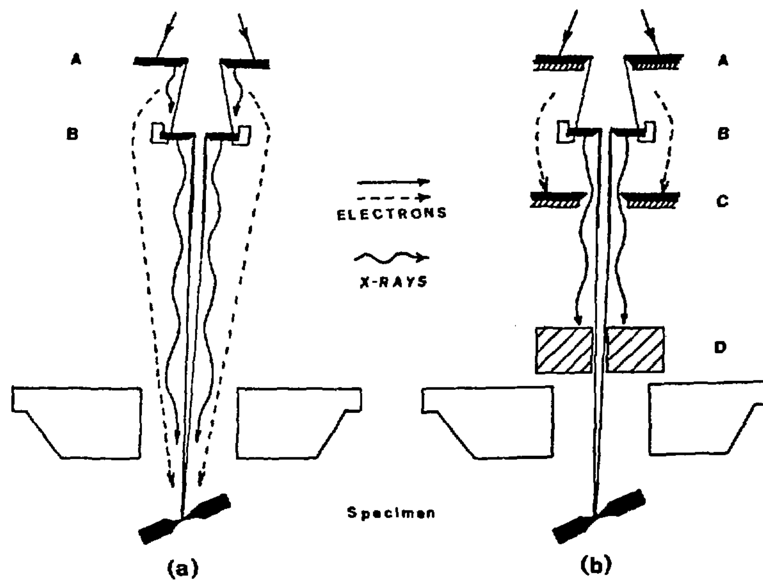

Figure 4.1. (a) Schematic illustration of remote sources of uncollimated fluorescing radiation from fixed (A) and variable(B) beam defining apertures. (b) Minimization techniques using thick fixed apertures (A) above the variable beam defining aperture (B), thick spray apertures (C) below the C_2 aperture, and non-beam defining apertures (D) just above the objective lens pole piece.

sample while the thin electron transparent region is confined to the edge of a small hole. The composition of the test specimen is also critical. The most pronounced effects are observed in specimens of medium-to-high atomic number elements (or homogeneous alloys) having both low energy (<3 keV) and medium energy (7 - 15 keV) characteristic x-ray emission lines. The latter since above 20 keV the detector efficiency decreases substantially. Suitable test specimens may be pure or alloyed molybdenum, zirconium, silver, or some of the homogeneous aluminum alloys such as β NiAl. These materials have the additional advantage that their emission lines are well separated from any systems peaks characteristic of the specimen holder material (usually copper).

In the remainder of this text we define the term "in-hole" spectrum as any x-ray spectrum detected when the incident electron probe is not impinging on the specimen. The origins of the "in-hole" spectrum are from the entire specimen and its environment excited by the uncollimated radiation. Even though this radiation may be weaker than the primary electron beam, it can produce measureable x-ray emission due to the large mass of material it fluoresces (diameters of several millimeters). It can be seen at once that uniformly thin films or extraction replicas minimize the amount of material which can undergo fluorescence.

There are essentially four steps in the elimination of remotely produced uncollimated radiation: (1) identification of the fluorescing species; (2) consultation with the instrument manufacturer concerning their solutions to the problem; (3) modifications to the electron optical column; and (4) corrections to measured spectra for quantitative analysis.

The identification of the fluorescing source is probably the most difficult task. The following sequence of tests is suggested (BENTLEY et al., 1979; GOLDSTEIN, 1978). First, examine the probe forming system to ascertain if it is possible for electrons to reach the specimen by scattering around the periphery of various apertures and holders. Second, with the variable condensor aperture holder in position and a thick solid disc in place of the normal aperture and attempt to detect the presence of any electron current at the specimen using a suitable Faraday cup and sensitive electrometer (note the currents may be ≤ 10 A). Third, acquire a representative in-hole spectrum with a suitable test specimen. If x-rays are the principle fluorescing source, the intensity of the low energy characteristic line should be extremely small relative to the medium energy line. Cross sections for fluorescence by x-ray photons favors excitation of the higher energy line. For example, the cross section ratio of Mo K_{α}/L_{α} for fluorescence by 60 keV x-ray photons is on the order to 200 while the ratio for Ni K_{α}/L_{α} is nearly 600. The same ratios for fluorescence by 100 keV electrons are on the order of 0.02. In addition, characteristic x-ray production will be due primarily to fluorescence deep within the sample and the lower energy line will undergo siginficant absorption relative to the higher energy line. In comparison, electron excitation favors the lower energy lines and x-ray generation will occur nearer the sample surface. Thus the ratio of the intensities of the high/low lines will be greater. A final test is to irradiate the bulk regions of the specimen with the probe. The overall characteristics of this electron excited spectrum can then be

compared qualitatively with the "in-hole" spectrum and these combined results will usually be sufficient to identify the source or sources.

The various manufacturers now offer a variety of modifications that reduce the magnitude of uncollimated radiation. These include: spray apertures above and below the variable (C2) drive assembly to reduce electron tails (SHUMAN et al., 1976), thick apertures in the probe forming system to reduce the emitted hard x-ray flux (JOY and MAHER, 1976) and thick (∿ mm) non-beam defining collimators between the condensor aperture system and the top of the objective lens pole piece (ZALUZEC and FRASER, 1976). Figure 4.1(b) illustrates these solutions. The prospective user is referred to a recent tutorial devoted to the subject for further details (BENTLEY et al., 1979).

Fluorescence effects by uncollimated radiation have been reported in a very wide variety of electron microscopes which were interfaced with an EDS system. However, the situation is largely correctable. The published data includes the following: Philips EM400 FEG (CARPENTER and BENTLEY, 1979); Philips EM400 (CLARKE, 1978); Philips EM301 (GEISS and HUANG, 1975; HREN et al., 1976); Philips EM300 (SHUMAN et al., 1976; GOLDSTEIN and WILLIAMS, 1977); JEOL 100B (JOY and MAHER, 1976); JEOL 100C (BENTLEY and KENIK, 1977); JEOL 100CX (HEADLEY and HREN, 1978); JEOL JSEM200 (ZALUZEC and FRASER, 1976); VG HB5 (FRASER, 1977); SIEMENS ST 100F (OPPOLZER and KNAUER, 1979); Hitachi H-700 (FIORI and JOY, 1979); Hitachi HU-1000 (ZALUZEC et al., 1978).

Hard x-ray fluorescence of the specimen and its environment has been identified in all of these instruments except the Siemons ST 100F, where the data were insufficient to unambiguously identify the sources. All of the Philips instruments exhibit substantial electron tails unless equipped with spray apertures above and below the variable C2.

Figure 4.2 shows an example of the reduction of the in-hole spectrum to an acceptable level (to be defined) in a modified AEM. The data presented were taken for an extreme case and should not be taken as representative of all microscopes or even newer models of the same manufacturer. The spectra shown in Figs. 4.2 (a) and (b) were obtained from the instrument "as received." The fluorescing source was identified as hard x-rays (ZALUZEC and FRASER, 1976) and satisfactorily reduced with an additional non-beam defining collimator (0.5 mm in diameter, 2 cm long) positioned just above the upper objective lens pole piece. Figs. 4.2 (c) and (d) show the equivalent spectra after modification. The in-hole signal was reduced by nearly two orders of magnitude. A substantial change in the relative Ni/Al K_α intensity ratio for the two cases is apparent.

The effect of the large in-hole spectrum on quantitative analysis is shown in Fig. 4.3. The measured intensity ratio of the Ni/Al K_α lines is plotted as a function of specimen thickness for the unmodified instrument (curve A) and for the calculated variation of the Ni/Al K_α intensity ratio (curve C). These calculations were based purely on electron excitation of the sample. Clearly, in the as-received state, the

thin film approximation is invalid and quantitative analysis is virtually impossible. The initial decrease of the Ni/Al ratio (Curve A) results from the increasing contribution of the electron probe excited signal with specimen thickness. As this signal begins to dominate and finally exceed that produced by the uncollimated radiation, the measured ratio will approach, but not necessarily reach, that corresponding to electron excitation. The remaining discrepancy will depend on the magnitude of the "in-hole" signal and may be substantial. The ratio eventually goes through a minimum, then begins to increase as absorption effects become important. Analagous trends will be observed if electron tails were the problem. The results of reduction of the uncollimated

Figure 4.2. Specimen (a) and in-hole (b) spectra obtained in an "as received" TEM/STEM JEOL JSEM 200 (1973). Test specimen β-NiAl disc. Modified stage. STEM mode, 200 keV, probe size 10 nm, specimen 100 nm thick, live time 200 sec. Specimen (c) and in-hole (d) spectra obtained in an AEM modified to reduce uncollimated fluorescing radiation. Note the changes relative to (a) and (b).

Figure 4.3. The effects of an in-hole signal on the measured intensity ratio in a NiAl alloy as a function of specimen thickness. A - as received instrument; B - modified instrument; C- calculated variation based on electron excitation model.

radiation on quantitative analysis is also shown in Fig. 4.3 (curve B). Agreement with theory is now much better. The discrepancy in the thinner regions of the foil is related to the detrimental aspects of contamination. Deviations in the last few data points can be attributed to errors in the thickness measurement and neglect of beam broadening effects in the calculations.

Ideally, one would like to completely eliminate the in-hole signal. Realistically this may be extremely difficult. A critical question is thus: At what level do we reach an acceptable in-hole signal? There is obviously no general answer to this question, but the following general

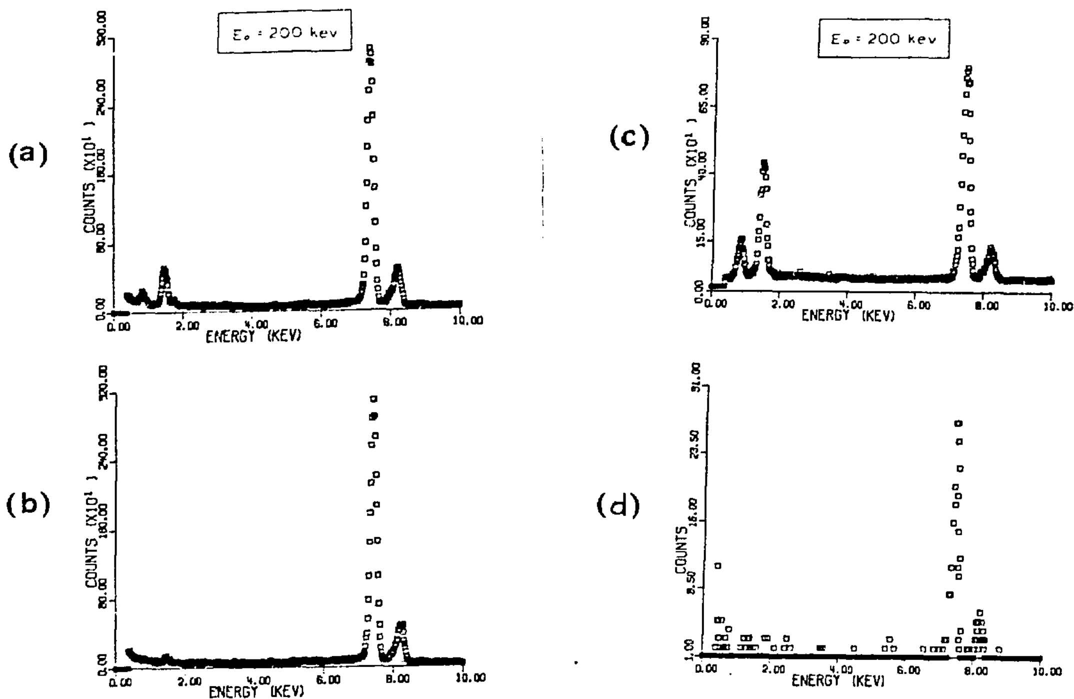

Figure 4.2. Specimen (a) and in-hole (b) spectra obtained in an "as received" TEM/STEM JEOL JSEM 200 (1973). Test specimen β-NiAl disc. Modified stage. STEM mode, 200 keV, probe size 10 nm, specimen 100 nm thick, live time 200 sec. Specimen (c) and in-hole (d) spectra obtained in an AEM modified to reduce uncollimated fluorescing radiation. Note the changes relative to (a) and (b).

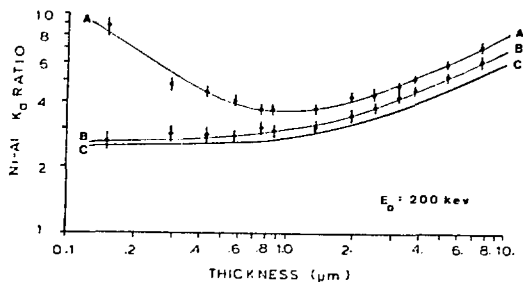

Figure 4.3. The effects of an in-hole signal on the measured intensity ratio in a NiAl alloy as a function of specimen thickness. A - as received instrument; B - modified instrument; C- calculated variation based on electron excitation model.

criterion seems reasonable. When the intensity of each characteristic x-ray line recorded during an "in-hole" measurement is less than 1% of the integrated intensity (FWHM) measured with the incident electron probe positioned on the thinnest area of the specimen to be studied, then the in-hole signal is deemed acceptable. Both spectra, of course, must be measured under identical operating conditions.

Even when we have obtained an acceptable in-hole signal, it is still necessary to correct all subsequent measurements for the small but detectable remaining spectrum. To good approximation, this may now be accomplished by simple subtraction of the remaining in-hole spectrum from each successive measurement (ZALUZEC and FRASER, 1977). An important assumption in this case is that the in-hole signal essentially remains constant over the same period of machine time as the sample measurement. It is also tacitly assumed that the locally produced radiation resulting from the interaction of the electron probe with the sample itself (see below) are important only to second order, and also that the remotely produced uncollimated radiation is directly related to the emission/probe current, which is taken to be constant. The latter, is a good approximation for thermionic guns; however, for instruments using Field Emission sources, this may be quite inaccurate. In the latter, the acquisition time may be controlled by a measurement of the integrated electron dose (FRASER and WOODHOUSE, 1978).

Four points should be remembered when applying an in-hole subtraction correction. First, the in-hole spectra will change from one specimen to another and thus should be measured for each specimen. Second, for each measurement one should acquire a corresponding in-hole spectrum so that long term changes in the emission/probe current do not invalidate the assumptions. Third, for trace element analysis extreme care must be taken to insure the statistical validity of minor peaks that may be detected both in the specimen and the in-hole data. Finally, it is essential to stress that the in-hole signal must be reduced before subtraction, otherwise additional errors may be introduced. Figure 4.4 is an example of the improper subtraction of the in-hole signal.

Figure 4.4. Subtraction of the in-hole signal to correct for uncollimated fluorescence. A - as received instrument; B - modified instrument with reduced in-hole signal subtracted; C - erroneous subtraction of in-hole signal without reduction of in-hole signal.

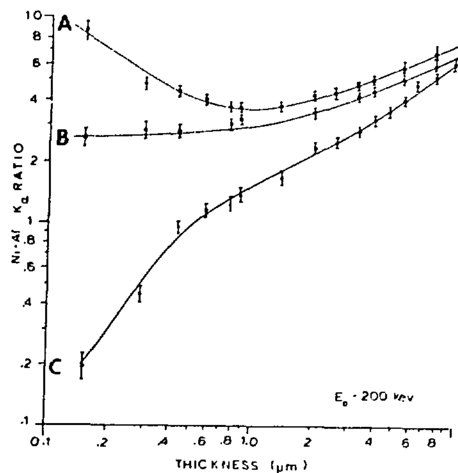

Figure 4.4. Subtraction of the in-hole signal to correct for uncollimated fluorescence. A - as received instrument; B - modified instrument with reduced in-hole signal subtracted; C - erroneous subtraction of in-hole signal without reduction of in-hole signal.

Fluorescence by Uncollimated Radiation: Local Sources

Fluorescence of the specimen and its immediate environment by locally produced radiation is also an important background source. Characteristic x-rays corresponding to the composition of the various support grids, goniometer stage, anti-contamination devices and other materials in the specimen chamber are all contributors. These local sources can sometimes affect quantitative analysis in particularly insidious ways. For simplicity, we will assume in this section that remote sources of uncollimated radiation have been minimized.

The primary source of local radiation is the specimen itself. As the focussed electron probe is scattered within the specimen secondary radiation from a multiplicity of sources is generated. The most significant components of this radiation include: backscattered and diffracted high energy electrons, specimen generated bremmstrahlung and characteristic x-rays.

The most noticable result of local fluorescence is the detection of x-rays which are characteristic of the environment. These x-ray photons will be detected simultaneously with the x-rays which are characteristic of the specimen. Due to the limited energy resolution of solid state x-ray detectors, the combined x-ray spectra may result in overlapping peaks. If the peak overlap problem is not too severe, individual peak intensities can be extracted using computerized data processing techniques. The worst case occurs when an element required in the analysis is also present in the system background. In this event, even quantitation analysis may be difficult and in some cases precluded.

Locally produced radiation can also fluoresce the specimen in the same manner as remotely produced radiation; however, its effects may be more subtle, for example, by selective enhancement of other elements in the specimen. An example is shown in Fig. 4.5 (BENTLEY et al., 1979), where one can immediately observe preferential fluorescence of the elements chronium and iron, relative to the nickel, by the copper K_α line systems peak. Such an effect is quite subtle, considering the apparently small copper systems peaks recorded. When the copper peaks were eliminated (Fig. 4.5a), the fluorescence effects are absent. In general, the specific type of specimen and its composition will influence greatly the magnitude of such fluorescence effects.

Complete elimination of locally generated radiation is virtually impossible; however, characteristic "systems peaks" from measured x-ray spectra can be effectively eliminated by surrounding the specimen with materials which do not generate detectable x-rays. Beryllium is without doubt the best materials choice, except for the potential machining hazards involved. An alternative material is graphite, but it suffers from poor mechanical strength. Regardless of the material chosen, a combination of the following modifications will substantially eliminate characteristic systems peaks.

Figure 4.5. Preferential fluorescence of Cr and Fe lines relative to Ni lines by Cu K systems peak. Specimen 316 stainless steel. Same area each spectrum. (a) Be double tilt gomometer (KENIK and BENTLEY, 1979). CuK lines minimized and fluorescent radiation absent. (b) Standard double tilt holder, copper alloy. CuK lines fluorescing Cr and Fe.

1. Low-atomic number specimen stages (SPRYS, 1975; LILJESVAN and ROOMANS, 1976; HREN et al., 1976; ZALUZEC and FRASER, 1976; NICHOLSON et al., 1977; KENIK and BENTLEY, 1979; HEADLEY and HREN, 1978; JOHNSON et al., 1978);

2. Beryllium and/or carbon coated plastic support grids (PANESSA et al., 1978);

3. Low-atomic number substitutes for the anti-contamination devices (HREN et al., 1976; NICHOLSON et al., 1977); and

4. Low-atomic number shields for the objective pole piece as well as modifications to the objective aperture blade (NICHOLSON et al., 1977).

Of these, the greatest improvements result from the use of low atomic number specimen stages and support grids. In any case, these modifications may not substantially affect the detection of systems generated continuum radiation, which may be important if the continuum intensity is monitored for use in quantitative analysis routines. In such cases, it will be necessary to employ a suitable correction scheme (ROBERTSON et al., 1978).

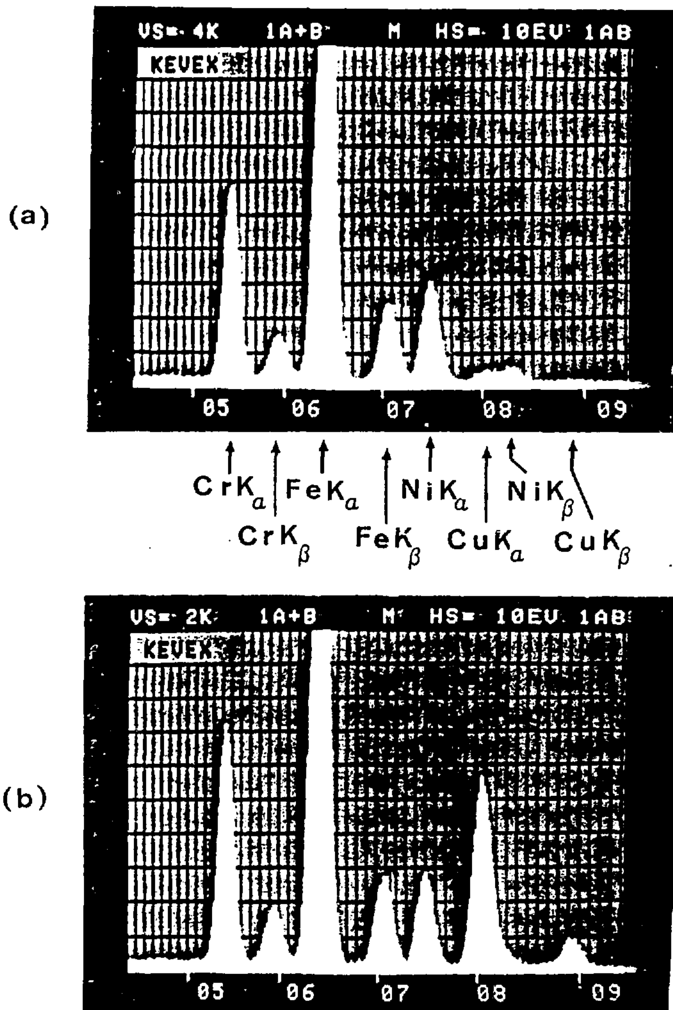

Figure 4.5. Preferential fluorescence of Cr and Fe lines relative to Ni lines by Cu K systems peak. Specimen 316 stainless steel. Same area each spectrum. (a) Be double tilt gomometer (KENIK and BENTLEY, 1979). CuK lines minimized and fluorescent radiation absent. (b) Standard double tilt holder, copper alloy. CuK lines fluorescing Cr and Fe.

Specimen Contamination

The mechanisms behind the accumulation of contamination as well as procedures for its reduction are important subjects in AEM and will be discussed in Chapter 18. As described there, its detrimental effects are not confined merely to image degradation. For completeness, we summarize here some of the effects of contamination on x-ray microanalysis.

Spatial resolution may be seriously degraded by beam broadening within the contaminant on the entrance surface. Thus, the beam striking the specimen is significantly larger than the microscope conditions would indicate. Space charging of the poorly conducting contaminant may further aggravate this problem (ZALUZEC and FRASER, 1977). The contaminant also contributes to the systems background in the continuum, in any case, and thereby decrease the attainable peak/background ratio. In turn, the minimum detectable limits are adversely affected (ZALUZEC and FRASER, 1977; SHUMAN et al., 1976). If the vacuum fluids contain silicon (or other elements with Z > 10), systems peaks may also be added. Finally, preferential adsorption in the contaminant of emitted x-rays from the specimen may occur for energy x-rays and thus directly affect quantitative analysis. On the positive side, contaminant deposits can serve as markers to indicate the approximate region analyzed, help to indicate problems of specimen drift, and may be used to measure the local thickness, since they mark both the top and bottom of the foil (see Chapter 18).

Detector Artifacts

Throughout the preceding discussion it has been tacitly assumed that a suitable solid state Si(Li) x-ray detector has been successfully interfaced to the column of the AEM, and that problems which are specific to such a device are not the limiting factors in analysis. There are, however, a set of artifacts directly linked to the detection and subsequent signal processing of x-ray emission spectra by these solid state detectors. The major artifacts associated with EDS detectors are listed below and the serious reader is referred to the literature for a detailed discussion of their effects and their minimization (FIORI and NEWBURY, 1978; REED, 1976; WOLDSETH, 1973); (1) detection efficiency; (2) generation of silicon escape peaks; (3) peak broadening and distortions; (4) formation of sum peaks due to pulse pile-up; (5) dead-time correction; and (6) microphonics.

4.4 OPTIMUM EXPERIMENTAL CONDITIONS FOR X-RAY ANALYSIS

The ultimate performance of x-ray microchemical analysis in an AEM requires optimization of the specific operating conditions used for the experimental measurements. In general, one wants to maximize the characteristic information measured from the specimen and minimize all other signals. The factors which influence the selection of operating conditions are discussed in this section. In all instances, it will be

assumed that the sample is thin enough to avoid complications resulting from electron scattering, x-ray absorption, and x-ray fluorescence. Furthermore, instrumental factors associated with uncollimated fluorescing radiation and sample contamination are assumed to be eliminated.

Detector/Specimen Geometry

Because of the variety of AEM instruments available, it is essential to take into account detector/specimen geometry and its effect on the sensitivity of x-ray analysis. Since all measures of sensitivity are related to the characteristic peak-to-background (P/B) ratio, it is used as a convenient evaluation parameter.

The emission of characteristic x-rays in a thin TEM sample is essentially isotropic. The continuum, on the other hand, is given off highly anisotropically and is strongly influenced by relativistic effects. The intensity of the continuum radiation I_c in the energy range between E_c and $E_c + dE_c$ emitted at an angle Ω with respect to the forward scattering direction (i.e., the incident beam direction) can be written as:

$$I_c(\Omega)\cdot dE_c\cdot d\Omega = \left[I_x\left\{\frac{\sin^2\Omega}{(1-\beta\cdot\cos\Omega)^4}\right\} + I_y\left\{1 + \frac{\cos^2\Omega}{(1-\beta\cdot\cos\Omega)^4}\right\}\right]\cdot k' \frac{dE_c}{E_c}\cdot d\Omega \quad (4.1)$$

where k' is a constant related to the sample thickness and composition and the parameters I_x and I_y are the continuum radiation components resulting from the deceleration of electrons in the specimen (SOMMERFELD, 1931; KIRKPATRICK and WIEDMANN, 1945). A polar plot of the angular distribution of continuum x-rays generated by 100 keV electrons incident on an infinitely thin specimen of nickel is shown in Fig. 4.6.

Figure 4.6. Anisotropic distribution of continuum radiation generated in a thin foil of nickel by a 100 keV electron beam. All intensities normalized to maximum. Forward scattering angle corresponds to observation at zero degrees. E_o - incident electron energy; E - continuum x-ray photon energy; Z - atomic number of specimen.

The optimum position of the detector can now be evaluated by calculating the (P/B) ratio as a function of Ω (ZALUZEC, 1978) as plotted in Fig. 4.7 for various incident beam energies. In all cases, the P/B

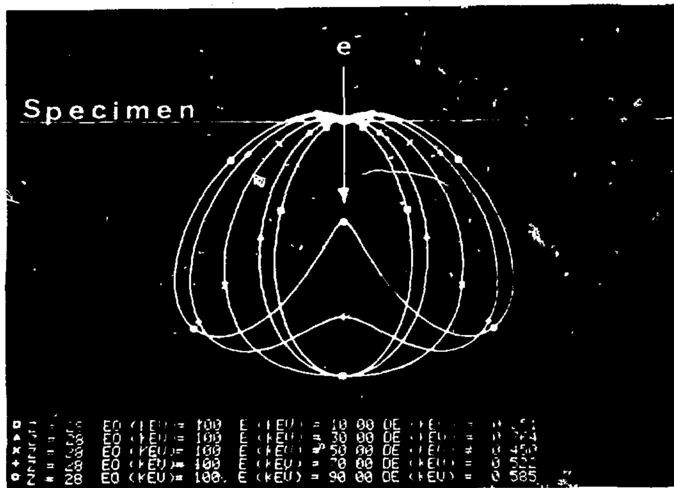

Figure 4.6. Anisotropic distribution of continuum radiation generated in a thin foil of nickel by a 100 keV electron beam. All intensities normalized to maximum. Forward scattering angle corresponds to observation at zero degrees. E_0 - incident electron energy; E - continuum x-ray photon energy; Z - atomic number of specimen.

ratio is maximized when the x-ray detector views the electron entrance surface at ($\Omega \geq \pi/2$). The variation in P/B begins to level out at angles above 125° (at 100 keV) which is being approached by several new commercial AEM instruments. The actual inclination of the specimen

Figure 4.7. Calculated peak-to-background ratio for a thin foil of nickel as a function of detector observation angle (Ω) at various incident electron beam energies. Z - atomic number of specimen; E - incident electron energy.

relative to the incident electron probe does not affect these calculations, for "thin" films. That is, even though the orientation of the specimen plane may be oblique to the incident beam the thin area under the focussed electron probe can be considered to be a segment of a horizontal thin slab. Of course, if the bremsstrahlung generated intercepts an appreciable mass, absorption effects will influence the calculated intensity. Such effects have been observed and shown to contribute to the "systems background" (GEISS and HUANG, 1975).

Detector Collimation

One of the principle advantages of EDS is the potentially large collection angle available. Due to their relatively compact size these detectors can usually be brought within ∿ 2 cm of the specimen and also results in a corresponding large subtended solid angle. The distinction between collection and subtending angles rests in the position of the apex of the respective solid angle cones, Fig. 4.8. The subtending solid angle is defined with the apex of its cone at the source point of the characteristic x-rays at the specimen. The collection solid angle

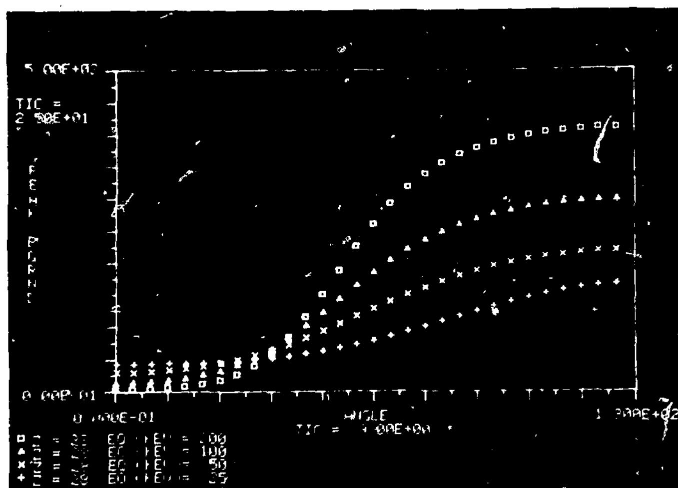

Figure 4.7. Calculated peak-to-background ratio for a thin foil of nickel as a function of detector observation angle (Ω) at various incident electron beam energies. Z - atomic number of specimen; E - incident electron energy.

is defined by the penumbra of the detector crystal and any collimators. If the solid state detector is simply mounted on the column of the AEM its large collection solid angle can result in the detection of "systems background" from the specimen environment as well as the specimen related x-rays. Because of this, collimators are usually positioned in front of the detector to restrict its field-of-view. These collimators also serve to reduce the flux of scattered electrons which also impinge on the detector and can introduce spectral artifacts or, if their energy is sufficiently high, actually damage the active area of the silicon crystal.

There is no universal design of collimator and therefore it is necessary to tailor its shape to a specific application. For example, in most studies one usually wants to maximize the specimen signal (thus, the subtending solid angle). On the other hand, the analysis of radioactive specimens requires minimization of the collection solid angle, since the specimen radioactivity can flood the signal processing chain. Most investigators want to maximize the detected specimen signal and minimize the "systems background," unfortuantely these two design requirements are mutually exclusive. A reasonable compromise can be obtained by constructing a collimator which maximizes the subtended solid angle and restricts the penumbra of the collimator cone (i.e., the collection solid angle) to an area at the specimen plane slightly larger than the actual specimen diameter. By using appropriate low-atomic number specimen stages, this relaxed condition on the collection solid angle will not contribute to a detection of characteristic systems peaks and will allow one to maximize the collection efficiency. The relationships between collimator geometry and the respective solid angles are given by STURCKEN, 1976.

Figure 4.8. Schematic illustration of collection solid angle (single hatched region) and subtended solid angle (cross-hatched) of an EDS detector in a TEM/STEM/AEM.

A final consideration is the choice of material to be used in collimator construction. High atomic number materials, such as tantalum or lead, are advantageous since they are effective x-ray shields; but, due to their high atomic number, there is a finite probability that scattering within the bore of the collimator can produce "systems peaks." This problem can be minimized by lining the inner bore with beryllium or graphite.

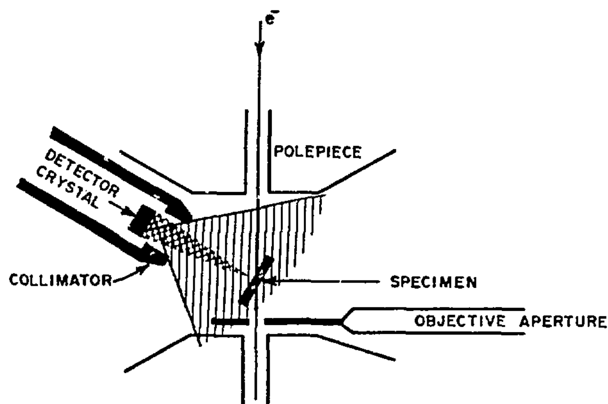

Figure 4.8. Schematic illustration of collection solid angle (single hatched region) and subtended solid angle (cross-hatched) of an EDS detector in a TEM/STEM/AEM.

Selection of Incident Beam Energy and Electron Source

Based on beam broadening effects (Chapter 3), it is apparent that it would be advantageous to increase the incident beam energy to the highest attainable level. Thus, there is considerable interest in performing x-ray microanalysis at energies greater than 100 keV. This becomes even more attractive since the sensitivity of x-ray analysis also increases with increasing energies (JOY and MAHER, 1977; ZALUZEC, 1978). Figure 4.10 plots the calculated P/B ratio generated by the electron excitation of a thin foil as a function of overvoltage (U) of the incident beam. There is a monotonic increase in the P/B ratio with incident electron energy which indicates that the optimum incident electron energy in an ideal AEM may indeed be the highest attainable.

Figure 4.9. Calculated peak-to-background ratio as a function of overvoltage U (= E_o/E_c). E_o - incident electron energy; E_c - x-ray absorption edge energy; Z - atomic number of specimen.

Unfortunately, the problems associated with uncollimated fluorescent radiation in the illuminating system also becomes more acute as the incident beam energy increases (ZALUZEC and FRASER, 1976; ZALUZEC et al., 1978; CLIFF et al., 1978). At accelerating voltages of 200 keV and less, the problems are correctable by the procedures previously outlined. Serious studies using HVEM based microanalysis have only recently been attempted (ZALUZEC et al., 1978, CLIFF et al., 1978). Although the problems are severe, workable solutions are apparently feasible. Further developmental work in the electron-optical system is still necessary in order to produce the required minute high-current density electron probes for HVEM systems to be useful in x-ray analysis.

No electron source will presently satisfy all the requirements of analytical electron microscopy. Each of the parameters which characterize the various emitters (source size, stability, brightness, energy spread, and coherence) must be evaluated and matched to the instrument and the proposed mode of operation. Table 4.1 summarizes representative values of the characteristic parameters for each of the three types of electron sources available: thermionic tungsten, LaB_6, and tungsten

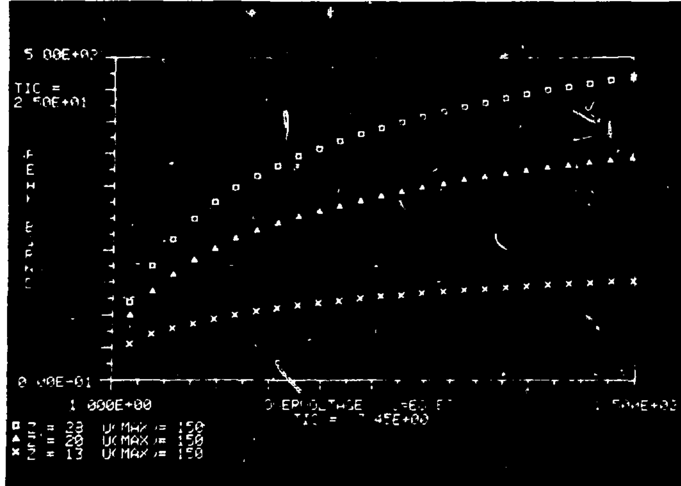

Figure 4.9. Calculated peak-to-background ratio as a function of overvoltage U (= E_o/E_c). E_o - incident electron energy; E_c - x-ray absorption edge energy; Z - atomic number of specimen.

field emission (JOY, 1977). The requirements for thin-foil x-ray microanalysis are quite simple: long and short term stability and maximum probe current (consistent with the limits set by beam heating and radiation damage). The attainable probe current directly affects the x-ray count rate. Its dependence as a function of probe diameter and emitter type are shown in Fig. 4.10. For high spatial resolution, one relies on the use of small probes and the FEG (field emission gun) appears to be the optimum choice. However, for TEM/STEM systems, where conventional transmission electron microscopy is also being performed, LaB_6 filaments may meet the wider range of desired analytical modes. Both these sources require better gun vacuums than do conventional tungsten hairpen filaments, thus increasing both the complexity and cost of the AEM system. Since overall improvements to the vacuum system are necessary to reduce specimen contamination, this disadvantage may soon disappear.

Figure 4.10. Typical probe current variation at the specimen with probe diameter for various electron sources.

Imaging and Diffraction Conditions During Analysis

A question often neglected before beginning an x-ray microanalysis is which imaging mode is most appropriate TEM or STEM? If probe sizes typical of TEM operation (5.0-0.2 μm) are sufficient to define the region of interest, then there is no need to resort to the potentially lower current STEM mode. For example, analysis of precipitates extracted on carbon replicas, where the precipitates are thin, large (200-500 nm), and well separated (spatially) may be advantageously analyzed by TEM instead of STEM. Even if the specimen requires a smaller probe, it is not always necessary to utilize STEM at its highest resolution.

Diffracting conditions may also play an important role in microanalysis. Both theoretical calculations and experimental measurements (HASHIMOTO et al., 1962; DUNCUMB, 1962; HALL, 1966; HUTCHINGS et al., 1978) indicate that anamolous increases in characteristic x-ray production (by as much as a factor of three), can result when thin crystalline foils are oriented in strongly diffracting conditions. These increases

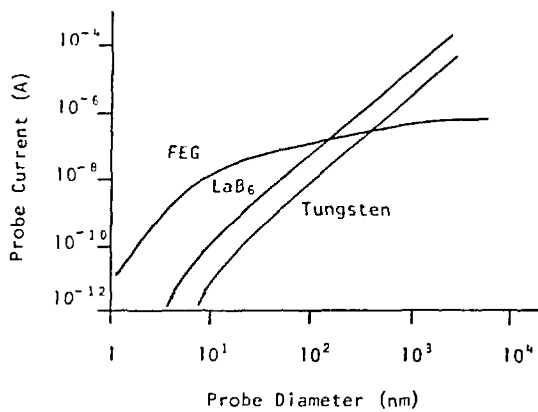

Figure 4.10. Typical probe current variation at the specimen with probe diameter for various electron sources.

Table 4.1

Comparison of Electron Sources

	SOURCE	β/Vo	SOURCE SIZE	ENERGY SPREAD (EV)	NOISE	STABILITY	COHERENCY	GUN VACUUM (TORR)
Thermionic	Tungsten Hairpin	1 $A/cm^2/sr/eV$	50 μm	~ 2	Low	Good	Low	$<10^{-4}$
	Pointed Filament	5	~10 μm	~ 2	Low	Fair	Moderate	$<10^{-5}$
LaB_6	Polycrystalline	10-30	~10 μm	< 1	Low	Good	Moderate	$<10^{-6}$
	Single Crystal	20-50	~ 5 μm	< 1	Low	Good	Moderate	$<10^{-6}$
Field Emission	Thermally Stabilized	100-500	~10 nm	~ 0.5	Fair ~ 1%	Moderate	High	$<10^{-8}$
	Cold	100-1000	~10 nm	~ 0.3	Fair ~ 1%	Fair	High	$<10^{-10}$

β is the source brightness in $A/cm^2/sr$, and Vo is accelerating potential in volts

result from asymmetries in the electron distribution of the Bloch waves and can be phenomenologically explained using a two beam dynamical model. In this approximation, one Bloch wave has nodes at the atom centers, while the node of the second wave will be between the reflecting planes. If the crystal is oriented such that the Bloch wave whose node is at the atom planes is highly excited (corresponding to a negative dynamical deviation parameter) then corresponding increases in characteristic x-ray emission are expected. The calculated variation in the relative probability (Q) of K shell excitation as a function of the deviation parameter is shown in Fig. 4.11 (HALL, 1966).

Such diffraction effects will not affect the validity of analysis if the region of the specimen being investigated is completely homogeneous and a standardless approach is being used. There are experiments where an erroneous analysis may result; for example, in quantitative analysis using thin film standards, when the intensity of either the unknown or the standard is affected. A particularly insidious effect may occur for composition profiles taken across an interface or of a precipitate embedded within a matrix. The diffraction conditions employed for imaging either the interface or the precipitate can be ideal for anamolous x-ray production. Thus, the combination of beam broadening and anamolous x-ray production can invalidate the assumptions of high spatial resolution and the quantitative interpretation of composition profiles.

The possible adverse effects of anamolous x-ray generation during analysis can be avoided if the specimen is oriented with a large positive (or negative) Bragg deviation parameter (w), or at any orientation where no low-order Bragg reflections are strongly excited. Some of the resulting loss in contrast in the images due to the "weak" diffracting conditions can be compensated by electronic signal processing.

Specimen Preparation Artifacts

The preparation of high quality thin specimens for transmission electron microscopy is an art in itself and is obviously important in all aspects of AEM based microanalysis. It is important to insure that these preparation techniques do not introduce artifacts to either the microstructure or the chemistry of the sample. Chemical or electrochemical thinning is potentially detrimental if proper precautions are not exercised. For example, contamination from the polishing solutions may remain on the sample surface and be subsequently detected as trace elements. The formation of oxide films (MORRIS et al., 1977) presents more subtle difficulties , since it may result in the formation of surface layers rich in a particular element. Ion-beam thinning can sometimes be used to remove such surface films, but it may of itself introduce microstructural changes or beam heating effects.

4.5 DATA REDUCTION FOR QUANTITATIVE ANALYSIS

The analysis of x-ray emission data obtained using an AEM based system can become a complex process. In addition to instrumental and

Figure 4.11. Calculated variation in the relative probability of K-shell excitation (Q) as a function of the dynamical deviation parameter (ω) (after HALL, 1966).

theoretical correction factors, one must also extract characteristic intensity measurements out of a spectrum of many peaks superimposed upon a slowly varying background. The major difficulty occurs in multi-element analysis, where there is spectral interference requiring deconvolution techniques. It is beyond the scope of this chapter to discuss the details of the various data manipulation techniques used; however, some of the salient considerations are described.

A general "rule-of-thumb" in choosing a data reduction technique is "simplest-is-best." Furthermore, there is no substitute for a good, clean spectrum containing a large number of counts in each channel. In such a spectrum there will be no need to employ elaborate smoothing functions or peak detection algorithms. If the statistical noise in a measured spectrum requires smoothing, then the operator should consider acquiring more data if possible as a first choice.

The following procedures for obtaining accurate x-ray information using an EDS system are suggested: (1) Acquire a spectrum from the region of interest. (2) Acquire in-hole data, and correct the sample spectrum appropriately. (3) Identify all characteristic peaks. (4) Subtract the background intensity. (5) Using suitable algorithms, obtain net peak intensities from all characteristic lines.

The use of "automatic" background correction routines is, in general, not recommended. These corrections usually rely on scaling a "standard" background curve to the measured specimen background. If the standard background has been produced under a different set of operating conditions (keV, geometry, thickness, etc.) it will not necessarily have the same characteristics as the background intensity measured from the specimen. A generalized polynomial function is adequate and can be analytically fitted to the background intensities (with appropriate modifications should an absorption edge be encountered). The function need not be based on any physical model, since we are interested only in obtaining integrated peak intensities. Similar consideration with respect to obtaining peak intensities by comparison to "standard" spectra also apply. Unless the standard spectra are acquired under identical operating conditions, they may not accurately duplicate the relevant peak

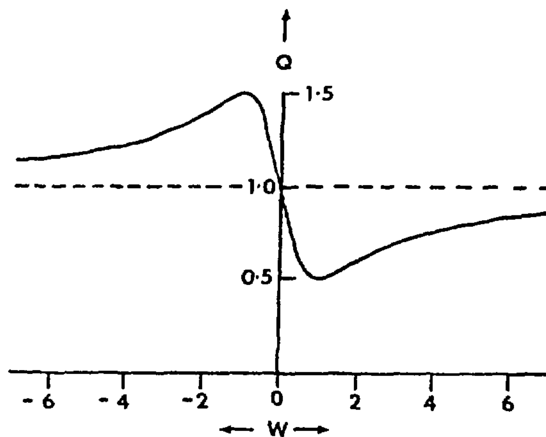

Figure 4.11. Calculated variation in the relative probability of K-shell excitation (Q) as a function of the dynamical deviation parameter (ω) (after HALL, 1966).

parameters (position, shape, and width) recorded during the specimen measurements, and thus can result in systematic errors.

It should also be pointed out that the quantitative routines require integrated peak intensities not peak heights. This distinction is important because a solid state detector system translates a fairly well defined x-ray line into a broad gaussian peak the width of which varies with the energy of the incident x-rays. Therefore, two x-ray lines of identical intensity (i.e., number of photons/sec) but of different energy will be recorded as gaussian peaks of equal area but different peak heights. This can be formulated by considering the integral (I) of a gaussian peak of standard deviation σ, and height H· which is given by

$$I = \int_{-\infty}^{+\infty} H \exp\left[-\frac{x^2}{2\sigma^2}\right] dx = \sqrt{2\pi} \cdot \sigma \cdot H \tag{4.2}$$

The ratio of the integrated intensities of the two different peaks is simply:

$$\frac{I_1}{I_2} = \frac{\sigma_1 \cdot H_1}{\sigma_2 \cdot H_2} \tag{4.3}$$

Clearly, only when $\sigma_1 = \sigma_2$ does the integrated peak ratio correspond to the peak height ratio. The use of a constant fraction of the total integrated intensity such as the integral over the full width of half maximum (FWHM) will not affect this intensity ratio.

4.6 APPLICATION OF QUANTITATIVE X-RAY MICROANALYSIS:

Parameters of Standardless Analysis

Since instrumental factors play such a large role in determining k it is risky to use data obtained from other instruments. As Goldstein points out in Chapter 3, there is a surprising paucity of published k values, considering popularity of the technique and the potential experimental errors associated with their measurement. Standardless analysis using calculated values of k is, in the author's view, a safer way to proceed. In Chapter 3, Goldstein reviews methods of such analyses following GOLDSTEIN et al. (1977). The present author has refined the selection of parameters in the examples presented at the end of this chapter (ZALUZEC, 1978). A brief summary is presented here.

The number of characteristic x-rays of element A (K_α or L_α) generated by electron excitation of a thin specimen of thickness dt can be written as:

$$\phi_A dt_A = Q_A \frac{N_o C_A}{A_A} \eta\, \omega_A\, a_A\, dt_A \tag{4.4}$$

Here Q_A is the ionization cross section of the K-shell (or L-shell) of element A; N_o, ρ, C_A, and A_A are, respectively, Avagadro's number, the sample density, the concentration in weight percent, and the atomic weight of A, η the number of electrons bombarding dt, ω_A the fluorescence yield of A and a_A the K_α fraction (e.g., $K_\alpha/K_\alpha + K_\beta$) of the total emission.

The corresponding x-ray intensity (I) which one measures can differ from this generated intensity because of the intrinsic efficiency of the detector. The relationship between the measured intensity (I) and the generated intensity (ϕ_A) is:

$$I_A = \varepsilon_A \phi_A \tag{4.5}$$

where ε is the efficiency of response of the detector system to the particular characteristic x-ray from element A. For solid state Si(Li) detectors this efficiency is a function of the energy of the given x-ray photon as well as the specific design parameters of the detector. In a general form, this efficiency can be represented by the following equation:

$$\varepsilon_A(E,\alpha) = \Pi_{j = Be,Au,Si} \left\{ \exp\left[-\left(\frac{\mu}{\rho}\right)_j^E \frac{\rho_j t_j}{\cos\alpha}\right]\right\}\left\{1-\exp\left[-\left(\frac{\mu}{\rho}\right)_{Si}^E \rho_{Si}\ t_{Si}^*\right]\right\} \tag{4.6}$$

The first term in brackets accounts for absorption of the incident x-ray photons before they reach the active region of the Si(Li) crystal and are detected. The product notation $\Pi\, j$=Be, Au, Si indicates that the sources of this absorption result from the cumulative effects of the beryllium window, gold conductive film, and silicon dead layer which spatially precede the active region of the detecting crystal. The term $(\frac{\mu}{\rho})_j^E$ is the mass absorption coefficient of the j element (i.e., Be, Au, Si) for an x-ray photon of energy E, while ρ , and t are respectively the mean density and thickness of each of these absorbers. Should the incident x-ray beam enter the detector inclined at an angle α with respect to its principal axis, then there is an effective increase in the mass thickness of each absorbing medium which is incorporated via the cos α term. If the incident x-ray energy is sufficiently high, then x-rays may be transmitted through the Si(Li) crystal. The corresponding loss in efficiency is accounted for by the second term in brackets, where as previously $(\frac{\mu}{\rho})_{Si}^E$ is the mass absorption coefficient for x-rays of energy E in silicon, ρ is the density of Si, and t^* is the thickness of the active region of the Si(Li) detecting crystal.

Combining these last three equations, one obtains the general relationship between the measured x-ray intensity I of a characteristic line of energy E and the local specimen composition:

$$I_A dt_A = \varepsilon_A(E_A,\alpha)\kappa_A C_A \eta_A dt_A \tag{4.7}$$

with

$$\kappa_A \equiv \frac{Q_A \omega_A a_A}{A_A} \tag{4.8}$$

An EDS system allows one to measure simultaneously most of the characteristic x-ray photons generated within the region of interest of the specimen and thus the ratio of any two-x-ray lines can be written as:

$$\frac{I_A dt_A}{I_B dt_B} = \frac{\varepsilon_A \kappa_A C_A \eta_A dt_A}{\varepsilon_B \kappa_B C_B \eta_B dt_B} \tag{4.9}$$

Since $\eta_A = \eta_B$ and $dt_A = dt_B$ for a thin film, Eqn. 4.9 simplifies to

$$\frac{I_A}{I_B} = \frac{\varepsilon_A \kappa_A C_A}{\varepsilon_B \kappa_B C_B} \tag{4.10}$$

which is equivalent to the Cliff-Lorimer equation (Chapter 3):

$$\frac{C_A}{C_B} = k_{AB} \frac{I_A}{I_B} \tag{4.11}$$

with

$$k_{AB} = \frac{\varepsilon_B \kappa_B}{\varepsilon_A \kappa_A} \tag{4.12}$$

The x-ray generation constant κ_A may be calculated to good precision for either K_α or L_α from a set of parameterized equations. It may be written in the following terms (for either K_α or L_α):

$$\kappa_A = \frac{Q_A \omega_A a_A}{A_A} \tag{4.13}$$

where A_A is the atomic weight and the other terms will be described below. The ionization cross section Q_A for the K shell is obtained from

$$Q_A(E_o) = \frac{\pi e^4 . Z_A . a(K)}{E_o \cdot E_C} \left\{ \ell n \left[b(K) \frac{E_o}{E_C} \right] - \ell n \ (1 - \beta^2) - \beta^2 \right\} \tag{4.14}$$

where

$$a(K) = 0.35, \; b(K) = \frac{0.2}{U_o \cdot \{1 - \exp(-\gamma)\} \cdot \{1 - \exp(-\delta)\}},$$

$$U_o = E_o/E_C \equiv \text{overvoltage ratio}, \; \delta = \tfrac{1}{2} \cdot E_C,$$

$$\gamma = \frac{1250}{E_A \cdot U_o^2}, \; \pi e^4 = 6.4924 \times 10^{20}, \quad \beta = \frac{v}{c}$$

and E_o, E_c are respectively the incident beam energy and the critical excitation energy of the element A. For application to L-shell analysis the constant a(L) is set equal to 0.25 and all other terms are replaced by their L-shell equivalents. When all energies are expressed in keV, the units of Q_A (E_o) are cm^2/atom.

The functions a(K) and b(K) given above were determined analytically (ZALUZEC, 1978) by fitting Eqn. 4.14 to measurements of Q for aluminum, nickel, and silver (HINK and ZIEGLER, 1969; POCKMAN et al., 1947; KIRKPATRICK and BAEZ, 1947). Figures 4.12 and 4.13 compare the predictions of this equation (solid curve) with experiment and with other calculated values.

Figure 4.12. Comparison of experimental ionization cross section as a function of overvoltage for nickel (squares) to various calculations. (1) Using Eqns. 4.14; (2), (3) due to POWELL, 1976; and (4) due to WORTHINGTON and TOMLIN, 1956.

Figure 4.13. Comparison of experimental ionization cross section as a function of overvoltage for silver (squares) to various calculations. (1) Using Eqns. 4.14; (2), (3) due to POWELL, 1976; and (4) due to WORTHINGTON and TOMLIN, 1956.

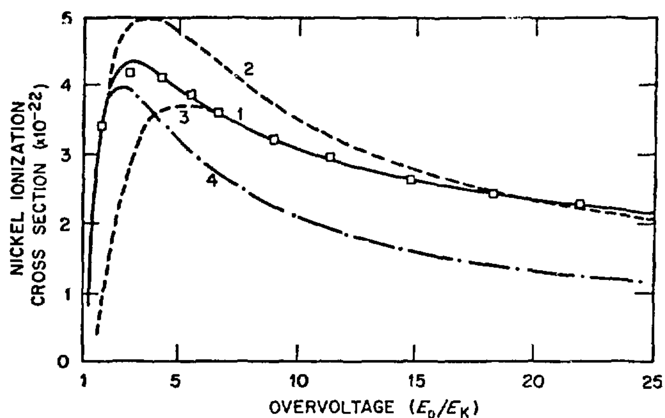

Figure 4.12. Comparison of experimental ionization cross section as a function of overvoltage for nickel (squares) to various calculations. (1) Using Eqns. 4.14; (2), (3) due to POWELL, 1976; and (4) due to WORTHINGTON and TOMLIN, 1956.

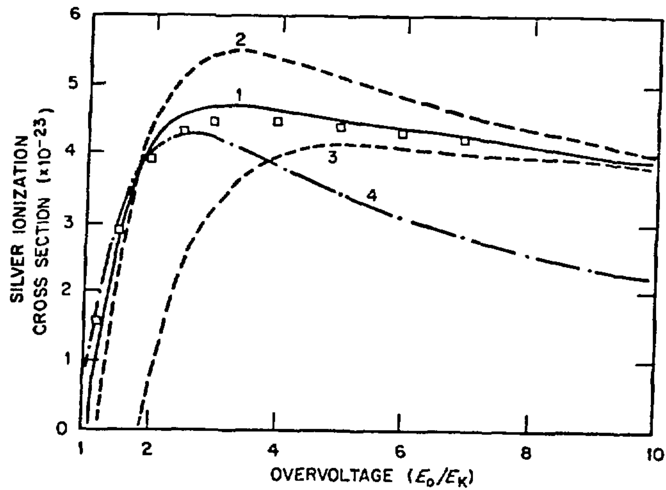

Figure 4.13. Comparison of experimental ionization cross section as a function of overvoltage for silver (squares) to various calculations. (1) Using Eqns. 4.14; (2), (3) due to POWELL, 1976; and (4) due to WORTHINGTON and TOMLIN, 1956.

The fluorescent yield ω_A can be calculated from the empirical expression,

$$\left|\frac{\omega_A}{1-\omega_A}\right|^{\frac{1}{4}} = A + BZ + CZ^3 \qquad (4.15)$$

in which the coefficients A, B, and C are fitted to experimental measurements (BURHOP, 1955; COLBY, 1968; DYSON, 1973). In this case, the periodic table is broken up into segments and a set of constants is used to determine ω for various ranges of Z. Since dedicated minicomputers are normally used for quantitative analysis, it is preferred to use Eqn. 4.15 (or tabulated values) rather than the expression by Wentzel (GOLDSTEIN, Chapter 3). The K_α fraction of the total K-shell emission a_A can be obtained from polynomial fits to experimental data or in tabulated form (SLIVINSKY and EBERT, 1972; HEINRICH, 1976; MCGUIRE, 1970; COLBY, 1968).

Tables 4.1, 4.2 and 4.3 document the calculated x-ray generation constants for K_α and L_α x-rays for incident electron energies of 100, 120, and 200 keV and over the range of atomic numbers $10 \leq Z \leq 92$. The constants for the K_α x-rays for elements with $Z \geq 58$ are omitted since their characteristic energies are greater than 40 keV. Similarly, the constants for L_α x-rays for elements with $Z \leq 30$ are omitted since their energies are less than 1.0 keV and their usage in quantitative analysis is not recommended. Table 4.4 also lists the calculated efficiency of a typical solid state detector between 0.6 and 20.0 keV. The detector parameters used in this calculation were: $t_{Be} = 7.6$ μm; $t_{Au} = 0.02$ μm; $t_{Si(dead\ layer)} = 0.1$ μm; $t_{Si(active\ crystal)} = 3.0$ mm.

There are, of course, alternate formulations which have been used to calculate the constant k_α of Eqn. 4.11. Figure 4.14 compares experimental measurements for 100 keV electrons of this constant (normalized to the silicon K_α line) for K_α (CLIFF and LORIMER, 1975) and L_α lines (GOLDSTEIN et al., 1977) with the predicted k factors using the present formulation (ZALUZEC, 1978) and an earlier parameterization by GOLDSTEIN et al. (1977).

Absorption Correction

The set of equations for the absorption correction in Chapter 3 are presented here in a more generalized parametric form. This formulation is not unique and an alternate formulation may be found in BENTLEY and KENIK (1979).

For the relatively simple geometry found in most electron microprobes, the electron beam strikes the specimen roughly normal to its surface (i.e. the geometry used in Chapter 3). The exiting path length d is then given by

Table 4.2

X-ray generation constant for 100 keV electrons: $\kappa_A = \frac{Q_A \cdot w_A \cdot a_A}{A_A}$

Z	κ^{K}_{α}	κ^{L}_{α}	Z	κ^{K}_{α}	κ^{L}_{α}
10	2.7180E-24	-	51	2.1296E-25	1.2838E-24
11	2.7565E-24	-	52	1.9439E-25	1.2285E-24
12	2.9429E-24	-	53	1.8813E-25	1.2374E-24
13	2.9386E-24	-	54	1.7629E-25	1.1967E-24
14	3.0806E-24	-	55	1.7029E-25	1.1817E-24
15	3.0081E-24	-	56	1.6272E-25	1.1418E-24
16	3.0935E-24	-	57	1.6071E-25	1.1260E-24
17	2.9158E-24	-	58	-	1.1123E-24
18	2.6527E-24	-	59	-	1.1010E-24
19	2.7625E-24	-	60	-	1.0695E-24
20	2.7312E-24	-	61	-	1.0426E-24
21	2.4531E-24	-	62	-	1.0117E-24
22	2.3057E-24	-	63	-	9.9252E-25
23	2.1584E-24	-	64	-	9.5014E-25
24	2.0930E-24	-	65	-	9.3046E-25
25	1.9497E-24	-	66	-	8.9980E-25
26	1.8773E-24	-	67	-	8.7584E-25
27	1.7321E-24	-	68	-	8.5245E-25
28	1.6844E-24	-	69	-	8.3233E-25
29	1.5007E-24	-	70	-	8.0066E-25
30	1.4002E-24	-	71	-	7.7955E-25
31	1.2551E-24	1.4375E-24	72	-	7.5169E-25
32	1.1482E-24	1.4546E-24	73	-	7.2877E-25
33	1.0559E-24	1.4770E-24	74	-	7.0440E-25
34	9.4805E-25	1.4618E-24	75	-	6.8249E-25
35	8.8402E-25	1.5004E-24	76	-	6.5512E-25
36	7.9359E-25	1.4805E-24	77	-	6.3518E-25
37	7.3100E-25	1.49703-24	78	-	6.1266E-25
38	6.6878E-25	1.5013E-24	79	-	5.9367E-25
39	6.1735E-25	1.5170E-24	80	-	5.6990E-25
40	5.6298E-25	1.5121E-24	81	-	5.4648E-25
41	5.1687E-25	1.5148E-24	82	-	5.2626E-25
42	4.6789E-25	1.4935E-24	83	-	5.0906E-25
43	4.2390E-25	1.4707E-24	84	-	4.9396E-25
44	3.8836E-25	1.4611E-24	85	-	4.8135E-25
45	3.5708E-25	1.4531E-24	86	-	4.4345E-25
46	3.2374E-25	1.4208E-24	87	-	4.2970E-25
47	2.9990E-25	1.4146E-24	88	-	4.1248E-25
48	2.7093E-25	1.3685E-24	89	-	3.9931E-25
49	2.5041E-25	1.3485E-24	90	-	3.7966E-25
50	2.2954E-25	1.3115E-24	91	-	3.7048E-25
			92	-	3.4912E-25

Table 4.3

X-ray generation constant for 120 keV electrons $\kappa = \frac{Q_A \cdot w_A \cdot a_A}{A_A}$

Z	κ^{K}_{α}	κ^{L}_{α}	Z	κ^{K}_{α}	κ^{L}_{α}
10	2.3966E-24	-	51	2.1092E-25	1.1699E-24
11	2.4386E-24	-	52	1.9305E-25	1.1210E-24
12	2.6121E-24	-	53	1.8729E-25	1.1306E-24
13	2.6170E-24	-	54	1.7586E-25	1.0949E-24
14	2.7525E-24	-	55	1.7014E-25	1.0826E-24
15	2.6966E-24	-	56	1.6275E-25	1.0474E-24
16	2.7820E-24	-	57	1.6078E-25	1.0342E-24
17	2.6306E-24	-	58	-	1.0229E-24
18	2.4008E-24	-	59	-	1.0138E-24
19	2.5079E-24	-	60	-	9.8608E-25
20	2.4869E-24	-	61	-	9.6242E-25
21	2.2403E-24	-	62	-	9.3506E-25
22	2.1117E-24	-	63	-	9.1845E-25
23	1.9824E-24	-	64	-	8.8028E-25
24	1.9277E-24	-	65	-	8.6308E-25
25	1.8005E-24	-	66	-	8.3562E-25
26	1.7382E-24	-	67	-	8.1432E-25
27	1.6080E-24	-	68	-	7.9349E-25
28	1.5677E-24	-	69	-	7.7566E-25
29	1.4002E-24	-	70	-	7.4700E-25
30	1.3098E-24	-	71	-	7.2813E-25
31	1.1769E-24	1.2729E-24	72	-	7.0291E-25
32	1.0793E-24	1.2898E-24	73	-	6.8224E-25
33	9.9495E-25	1.3115E-24	74	-	6.6017E-25
34	8.9551E-25	1.2999E-24	75	-	6.4036E-25
35	8.3709E-25	1.3361E-24	76	-	6.1537E-25
36	7.5332E-25	1.3204E-24	77	-	5.9731E-25
37	6.9565E-25	1.3370E-24	78	-	5.7677E-25
38	6.3805E-25	1.3429E-24	79	-	5.5952E-25
39	5.9050E-25	1.3589E-24	80	-	5.3774E-25
40	5.3992E-25	1.3564E-24	81	-	5.1621E-25
41	4.9704E-25	1.3608E-24	82	-	4.9768E-25
42	4.5118E-25	1.3437E-24	83	-	4.8196E-25
43	4.0992E-25	1.3251E-24	84	-	4.6820E-25
44	3.7664E-25	1.3184E-24	85	-	4.5677E-25
45	3.4733E-25	1.3130E-24	86	-	4.2129E-25
46	3.1585E-25	1.2857E-24	87	-	4.0871E-25
47	2.9348E-25	1.2819E-24	88	-	3.9279E-25
48	2.6595E-25	1.2419E-24	89	-	3.8070E-25
49	2.4656E-25	1.2255E-24	90	-	3.6240E-25
50	2.2669E-25	1.1935E-24	91	-	3.5407E-25
			92	-	3.3407E-25

Table 4.4

X-ray generation constant for 200 keV electrons: $\kappa = (Q \cdot w \cdot a)/A_A$

Z	κ^{K}_{α}	κ^{L}_{α}	Z	κ^{K}_{α}	κ^{L}_{α}
10	1.6659E-24	-	51	1.9705E-25	8.8218E-25
11	1.7089E-24	-	52	1.8131E-25	8.4826E-25
12	1.8455E-24	-	53	1.7672E-25	8.5849E-25
13	1.8640E-24	-	54	1.6659E-25	8.3421E-25
14	1.9765E-24	-	55	1.6165E-25	8.2764E-25
15	1.9519E-24	-	56	1.5491E-25	8.0343E-25
16	2.0299E-24	-	57	1.5313E-25	7.9599E-25
17	1.9346E-24	-	58	-	7.8991E-25
18	1.7795E-24	-	59	-	7.8547E-25
19	1.8732E-24	-	60	-	7.6650E-25
20	1.8718E-24	-	61	-	7.5056E-25
21	1.6988E-24	-	62	-	7.3160E-25
22	1.6133E-24	-	63	-	7.2094E-25
23	1.5256E-24	-	64	-	6.9322E-25
24	1.4943E-24	-	65	-	6.8185E-25
25	1.4057E-24	-	66	-	6.6228E-25
26	1.3667E-24	-	67	-	6.4746E-25
27	1.2732E-24	-	68	-	6.3291E-25
28	1.2500E-24	-	69	-	6.2066E-25
29	1.1242E-24	-	70	-	5.9963E-25
30	1.0589E-24	-	71	-	5.8633E-25
31	9.5813E-25	8.9402E-25	72	-	5.6782E-25
32	8.8471E-25	9.0904E-25	73	-	5.5287E-25
33	8.2126E-25	9.2755E-25	74	-	5.3668E-25
34	7.4433E-25	9.2260E-25	75	-	5.2222E-25
35	7.0063E-25	9.5166E-25	76	-	5.0343E-25
36	6.3494E-25	9.4377E-25	77	-	4.9022E-25
37	5.9047E-25	9.5910E-25	78	-	4.7487E-25
38	5.4541E-25	9.6676E-25	79	-	4.6214E-25
39	5.0836E-25	9.8182E-25	80	-	4.4556E-25
40	4.6813E-25	9.8358E-25	81	-	4.2910E-25
41	4.3404E-25	9.9035E-25	82	-	4.1503E-25
42	3.9682E-25	9.8139E-25	83	-	4.0322E-25
43	3.6311E-25	9.7130E-25	84	-	3.9297E-25
44	3.3602E-25	9.6987E-25	85	-	3.8463E-25
45	3.1207E-25	9.6941E-25	86	-	3.5592E-25
46	2.8578E-25	9.5258E-25	87	-	3.4642E-25
47	2.6737E-25	9.5320E-25	88	-	3.3403E-25
48	2.4392E-25	9.2668E-25	89	-	3.2482E-25
49	2.2760E-25	9.1768E-25	90	-	3.1024E-25
50	2.1056E-25	8.9687E-25	91	-	3.0411E-25

Table 4.5

Detector Efficiency $\varepsilon(E,\alpha)$

E(keV)	α - 0°	α - 20°	E(keV)	α - 0°	α - 20°
0.60	0.0274	0.0218	10.40	0.9942	0.9939
0.80	0.1945	0.1751	10.60	0.9945	0.9942
1.00	0.4094	0.3866	10.80	0.9948	0.9945
1.20	0.5795	0.5595	11.00	0.9950	0.9947
1.40	0.6973	0.6814	11.20	0.9953	0.9950
1.60	0.7747	0.7621	11.40	0.9954	0.9952
1.80	0.8298	0.8199	11.60	0.9950	0.9954
2.00	0.8159	0.8054	11.80	0.9957	0.9956
2.20	0.8520	0.8433	12.00	0.9917	0.9913
2.40	0.7749	0.7624	12.20	0.9919	0.9916
2.60	0.8158	0.8052	12.40	0.9921	0.9918
2.80	0.8340	0.8243	12.60	0.9921	0.9920
3.00	0.8611	0.8528	12.80	0.9921	0.9921
3.20	0.8677	0.8598	13.00	0.9921	0.9922
3.40	0.8872	0.8804	13.20	0.9919	0.9921
3.60	0.8927	0.8862	13.40	0.9915	0.9920
3.80	0.9071	0.9014	13.60	0.9911	0.9917
4.00	0.9190	0.9141	13.80	0.9887	0.9894
4.20	0.9290	0.9246	14.00	0.9880	0.9890
4.40	0.9374	0.9335	14.20	0.9871	0.9884
4.60	0.9445	0.9411	14.40	0.9848	0.9863
4.80	0.9506	0.9475	14.60	0.9836	0.9855
5.00	0.9558	0.9531	14.80	0.9821	0.9844
5.20	0.9604	0.9579	15.00	0.9805	0.9831
5.40	0.9643	0.9620	15.20	0.9785	0.9816
5.60	0.9677	0.9656	15.40	0.9764	0.9799
5.80	0.9707	0.9688	15.60	0.9740	0.9780
6.00	0.9733	0.9716	15.80	0.9713	0.9758
6.20	0.9756	0.9741	16.00	0.9683	0.9734
6.40	0.9777	0.9762	16.20	0.9651	0.9707
6.60	0.9795	0.9782	16.40	0.9616	0.9678
6.80	0.9811	0.9799	16.60	0.9579	0.9646
7.00	0.9826	0.9815	16.80	0.9539	0.9611
7.20	0.9839	0.9829	17.00	0.9496	0.9574
7.40	0.9851	0.9841	17.20	0.9450	0.9535
7.60	0.9861	0.9853	17.40	0.9402	0.9493
7.80	0.9871	0.9863	17.60	0.9351	0.9448
8.00	0.9880	0.9872	17.80	0.9298	0.9401
8.20	0.9888	0.9881	18.00	0.9243	0.9351
8.40	0.9895	0.9888	18.20	0.9185	0.9299
8.60	0.9902	0.9896	18.40	0.9125	0.9245
8.80	0.9908	0.9902	18.60	0.9062	0.9188
9.00	0.9914	0.9908	18.80	0.8998	0.9130
9.20	0.9919	0.9914	19.00	0.8932	0.9069
9.40	0.9923	0.9919	19.20	0.8863	0.9006
9.60	0.9928	0.9923	19.40	0.8794	0.8942
9.80	0.9932	0.9927	19.60	0.8722	0.8875
10.00	0.9936	0.9931	19.80	0.8649	0.8807
10.20	0.9939	0.9935	20.00	0.8574	0.8738

Figure 4.14. A comparison of experimental measurements with calculations of the constant k_{XXSi} for K_α lines (a) and L_α lines (b) of various elements. Incident electron energy 100 keV.

$$d = t \cdot \text{cosec}\ \theta_E \tag{4.16}$$

where t is the depth of production and θ_E is the take-off angle. Because of the constraints on detector size and position imposed by the objective lens pole piece, the geometry found in an AEM is not so simple. The x-ray geometry found on a general analytical electron microscope is shown in Fig. 4.15 which represents a plane section through the sample containing the incident beam direction and the detector axis. The elevation angle, θ_E, is defined relative to an imaginary plane perpendicular to the incident beam direction and is nominally located at the height of the midplane of the untilted specimen. From this figure, one can show that the relationship between depth of production and exiting path length is now given by:

$$d = t \cdot \frac{\sin \beta}{\cos(\beta - \theta_E)} \equiv t \cdot f\ (\beta, \theta) \tag{4.17}$$

For the special case of normal incidence ($\beta = \pi/2$), Eqn. 4.17 reduces to Eqn. 4.16. Care must be taken in using Eqn. 4.17 on samples which are severely bent or having significant thickness changes over the area being analyzed. The angle of electron incidence, β, is also a function of the detector/specimen geometry. It is convenient to plot the various parameters on a stereographic projection from which the value of β can easily be read (ZALUZEC, 1978) but can also be obtained using solid geometry.

(a)

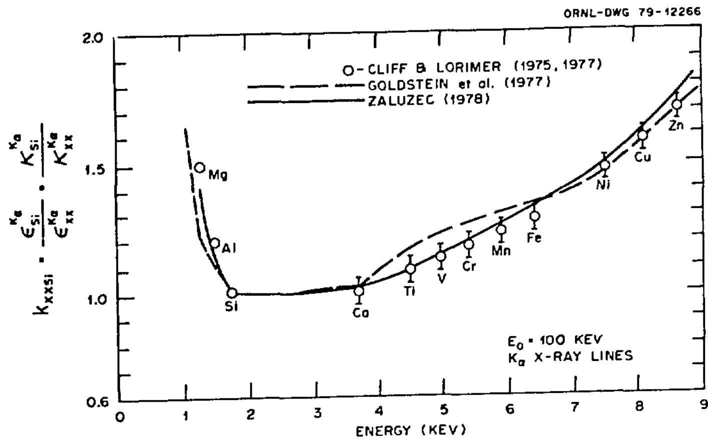

(b)

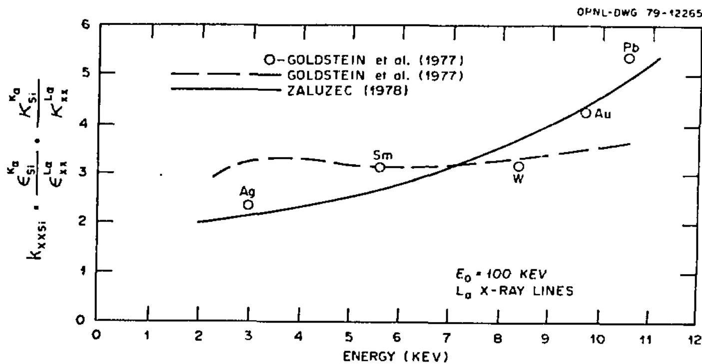

Figure 4.14. A comparison of experimental measurements with calculations of the constant k_{XXSi} for K_α lines (a) and L_α lines (b) of various elements. Incident electron energy 100 keV.

Figure 4.15. Geometry of the absorption correction in an AEM.

The total characteristic intensity (K_α or L_α) emitted in the direction of the detector system, including absorption effects, is given by:

$$\phi_A = \int_0^{t_o} \phi(t) \left\{ \exp \left[- \left(\frac{\mu}{\rho}\right)_{AB}^{A} \cdot \rho \cdot d \right] \right\} dt \qquad (4.18)$$

If one assumes $\phi(t)$ is nearly constant, Eqn. 4.18 can be solved to give:

$$\phi_A = \phi_A(0) \left\{ \frac{1-\exp \left[- \left(\frac{\mu}{\rho}\right)_{AB}^{A} \cdot \rho \cdot f(\beta,\theta) \; t_o \right]}{\left(\frac{\mu}{\rho}\right)_{AB}^{A} \cdot \rho \cdot f(\beta,\theta)} \right\} \qquad (4.19)$$

where ϕ (0) is the generation function evaluated at zero thickness. One can then easily show that:

$$\frac{C_A}{C_B} = \frac{\varepsilon_B \; \kappa_B \; \delta_B \; I_A}{\varepsilon_A \; \kappa_A \; \delta_A \; I_A} \qquad (4.20)$$

where the ratio δ_B / δ_A simplifies to

$$\frac{\delta_B}{\delta_A} = \left\{ \frac{\left(\frac{\mu}{\rho}\right)_{AB}^{A}}{\left(\frac{\mu}{\rho}\right)_{AB}^{B}} \right\} \cdot \left\{ \frac{1-\exp \left[- \left(\frac{\mu}{\rho}\right)_{AB}^{B} \cdot \rho \cdot f(\beta,\theta) \cdot t_o \right]}{1-\exp \left[- \left(\frac{\mu}{\rho}\right)_{AB}^{A} \cdot \rho \cdot f(\beta,\theta) \cdot t_o \right]} \right\} \qquad (4.21)$$

It should be noted that if $\beta = \pi/2$, this equation reduces to the result presented in Chapter 3.

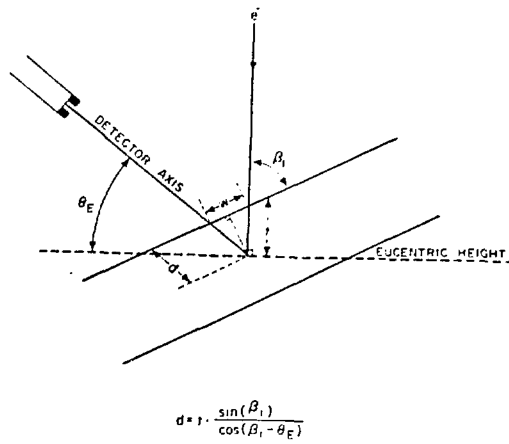

Figure 4.15. Geometry of the absorption correction in an AEM.

In order to calculate an absorption correction one needs to know the value of the mass absorption coefficient for K_α x-ray photons of element A of the alloy AB which is given by the equation:

$$\left(\frac{\mu}{\rho}\right)^A_{AB} = \sum_{i=1}^{N} \left(\frac{\mu}{\rho}\right)^A_i C_i \qquad (4.22)$$

In this expression C_i is the composition in weight percent of the i element in the sample and $(\frac{\mu}{\rho})^A_i$ is the absorption coefficient for the K_α or L_α x-ray of A in the pure element i. Obviously, the composition of the alloy is initially an unknown quantity; and, it is therefore necessary to determine $(\frac{\mu}{\rho})^A_{AB}$ iteratively. As a first approximation, the composition of the alloy is determined ignoring absorption effects. A first-order absorption correction is then calculated and new values of composition are then substituted into the absorption term and the procedure repeated until a suitable convergence is obtained.

These equations are of course only valid for a homogeneous sample of thickness t_o. The application of an absorption correction to an inhomogeneous sample is extremely difficult without some prior knowledge as to the relative composition and thickness of each phase in the excited volume. Thus, in such a situation one usually resorts to analysis of thinner regions of the sample which can be then considered locally homogeneous.

The criterion used to test the validity of the thin-film approximation can be still written in the form suggested by TIXIER and PHILIBERT (1969), that is, for all characteristic x-ray lines from which quantitative results are desired the product of $\chi_A \cdot \rho \cdot t$ must be less than 0.1. In this context χ_A is now defined as

$$\chi_A = \left(\frac{\mu}{\rho}\right)^A_{AB} \frac{\sin\beta}{\cos(\beta-\theta_E)} \qquad (4.23)$$

where all terms in Eqn. 4.23 have their previous definitions. Thus, if the condition

$$\chi_A \cdot \rho \cdot t < 0.1 \qquad (4.24)$$

fails for an x-ray line then the thin-film approximation is invalid and absorption effects must be included within the analysis scheme.

4.7 APPLICATIONS OF STANDARDLESS ANALYSIS

The analysis of homogeneous single phase regions using the standardless approach outlined in the preceding section is a simple procedure. This section will illustrate its application through several examples in an optimized AEM. All data presented in the remainder of this chapter

has, therefore, been obtained under low contamination rate conditions and has been appropriately corrected for any residual effects of uncollimated fluorescing radiation. The intensities (or intensity ratios) reported were obtained by integrating gaussian peak profiles (GEISS and HUANG, 1975) over their FWHM after a fitted specimen background curve has been subtracted from all measurements. In all cases the α line intensities reported consists of the sum of $\alpha_1 + \alpha_2$ components.

Table 4.6 compares the determination of the specimen composition using the thin-film standardless technique just outlined with bulk specimen compositions for several well characterized systems. For quantitative analysis using only K shell characteristic x-rays the agreement is excellent. Quantitative analysis using a combination of K and L shell emission lines is more tenuous, owing to the lack of accurate values for the ionization cross-section in the incident energy range typical of AEM studies. However, the use of the parameterized equations just developed yields results which are remarkably good considering the assumptions made in extending the K-shell formulation to L shell excitation. An example of such K-shell/ L-shell analysis can be seen by reference to the Ni_4Mo results of Table 4.6. In this instance, it was possible to measure the intensities of the Mo K_α, Ni K_α, and Mo L_α x-ray lines simultaneously and although it was necessary to deconvolute the Mo L_α line from the unresolved Mo $L_{\alpha+\beta}$ peak agreement between K-K and K-L analysis is good. Also included in this table is the result of L-shell analysis using only the L lines (Nb and Hf) and once again reasonable agreement is obtained. Two examples of quantitative x-ray analysis using the standardless technique are demonstrated below in greater detail.

Standardless Analysis Using the Thin-Film Approximation: Fe-13r-40Ni

This example will consider the application of standardless analysis in the thin-film approximation (i.e., absorption and fluorescence effects are negligible) to a homogeneous Fe-Cr-Ni specimen. X-ray measurements were made in the STEM mode of operation and a region of the specimen less than 200 nm thick was analyzed using ∿ 20 nm diameter probe at an incident energy of 120 keV. After correction for the presence of uncollimated fluorescing radiation, the measured characteristic K_α intensity ratios were:

$$\frac{I_{Fe}}{I_{Ni}} = 1.25 \text{ and } \frac{I_{Cr}}{I_{Ni}} = 0.46$$

The efficiency of the solid state x-ray detector used during these measurements can be obtained from Table 4.5 ($\alpha = 0°$), and the values for the x-ray generation constants from Table 4.3. Substituting the values for these parameters into Eqns. 4.11 and 4.12 one obtains the following relative composition ratios:

Table 4.6

Sample	Incident Energy (keV)	Measured Intensity I_{A}/I_{B}	Generated Intensity ϕ_{A}/ϕ_{B}	Ratio of X-Ray Generation Constants κ_{B}/κ_{A} $\kappa \equiv \frac{Q \cdot w \cdot a}{A}$	Composition: Thin Film X-ray Analysis	Composition: Bulk Analysis (wt%)
βNiAl	200.	$NiK_{\alpha}/AlK_{\alpha}$ = 2.05	1.53	1.491	Ni = 69.5 Al = 30.5	Ni - 68.5 Al - 31.5
	100.	$NiK_{\alpha}/AlK_{\alpha}$ = 1.79	1.34	1.744	Ni = 69.9 Al = 30.1	Ni = 68.5 Al = 31.5
β ZrNb	200.	$NbK_{\alpha}/ZrK_{\alpha}$ = 0.163	0.163	1.079	Nb = 14.9 Zr = 84.0	Nb = 15.4 Zr = 84.6
β CuZn	100	$CuK_{\alpha}/ZnK_{\alpha}$ = 1.63	1.634	0.933	Cu = 60.4 Zn = 39.6	Cu = 60.2 Zn = 39.8
Ni_4Mo	120	$MoK_{\alpha}/NiK_{\alpha}$ = 0.113	0.118	3.475	Mo = 29.2 Ni = 70.8	Mo = 29.0 Ni = 71.0
	120.	$MoL_{\alpha}/NiK_{\alpha}$ = 0.246	0.323	1.167	Mo = 27.4 Ni = 72.6	Mo = 29.0 Ni = 71.0
NbHf	120.	$NbL_{\alpha}/HfL_{\alpha}$ = 1.30	1.515	0.516	Nb = 43.9 Hf = 56.1	Nb = 45.9 Hf = 54.1
Fe-13Cr-40Ni	120	$FeK_{\alpha}/NiK_{\alpha}$ = 1.25	1.26	0.902	Ni = 40.1 Cr = 14.2 Fe = 45.7	Ni = 40.4 Cr = 13.2 Fe = 46.6
	120	$CrK_{\alpha}/NiK_{\alpha}$ = 0.426	0.435	0.813		
Fe-13Cr-20Ni	120.	$FeK_{\alpha}/NiK_{\alpha}$ = 3.59	3.619	0.902	Ni = 20.0 Cr = 14.5 Fe = 65.5	Ni = 19.7 Cr = 13.3 Fe = 66.9
	120.	$CrK_{\alpha}/NiK_{\alpha}$ = 0.0880	0.899	0.813		

$$\frac{C_{Fe}}{C_{Ni}} = \frac{\varepsilon_{Ni}\ \kappa_{Ni}\ I_{Fe}}{\varepsilon_{Fe}\ \kappa_{Fe}\ I_{Ni}} = \frac{0.9855}{0.9777} \cdot \frac{1.5677\times10^{-24}}{1.7382\times10^{-24}} \cdot (1.25) = 1.14$$

and

$$\frac{C_{Cr}}{C_{Ni}} = \frac{\varepsilon_{Ni}\ \kappa_{Ni}\ I_{Cr}}{\varepsilon_{Cr}\ \kappa_{Cr}\ I_{Ni}} = \frac{0.9855}{0.9643} \cdot \frac{1.5677\times10^{-24}}{1.9277\times10^{-24}} \cdot (0.426) = 0.354$$

Using the relationship that $\Sigma\ C_i = 100$, one solves for the compositions and obtains $C_{Ni} = 40.0$, $C_{Fe} = 45.7$, and $C_{Cr} = 14.2$ in excellent agreement with the bulk analysis.

Very similar answers are calculated using k_{AB} factors for K_α as discussed in Chapter 3. Using Eqns. 3.9, 3.10 and 3.14, k_{FeNi} and k_{CrNi} at 120 KV are 0.928 and 0.863 respectively. Since no absorption correction is made,

$$\frac{C_{Fe}}{C_{Ni}} = k_{FeNi}\ \frac{I_{Fe}}{I_{Ni}} = (0.928)(1.25) = 1.16$$

$$\frac{C_{Cr}}{C_{Ni}} = k_{CrNi}\ \frac{I_{Cr}}{I_{Ni}} = (0.863)(0.426) = 0.354$$

Upon substitution of the values for C_{Fe}/C_{Ni} and C_{Cr}/C_{Ni} as above, one obtains (in wt %): $C_{Ni} = 39.6$, $C_{Fe} = 45.9$ and $C_{Cr} = 14.5$. Both calculation schemes yield compositions which fall well within the known error limits of the measured intensity ratios, I_{Fe}/I_{Ni} and I_{Cr}/I_{Ni}. The agreement between the two formulations is obviously quite reasonable; however, the analysis based on the L-shell differ significantly (see Fig. 4.14).

Standardless Analysis Using the Absorption Correction: β NiAl

The preceding example dealt with quantitative analysis in the thin-film approximation, in this illustration the application of the absorption correction to standardless analysis will be demonstrated. A homogeneous single crystal specimen of β NiAl ($C_{Ni} = 68.5$; $C_{Al} = 31.5$ wt%; $\rho = 5.9$ gms/cm^3) was analyzed at 200 keV in STEM using a probe diameter ~ 20 nm. A characteristic K_α intensity ratio of Ni/Al, of 2.80 was subsequently measured from a region of the specimen ~ 425 nm thick after correction for the residual in-hole spectrum. During these measurements the detector elevation angle θ_E was 0° while the electron incident angle

was $\beta \sim 45°$. Using the conventional thin-film analysis equations one obtains a composition ratio.

$$\frac{C_{Ni}}{C_{Al}} = \frac{\varepsilon_{Al}}{\varepsilon_{Ni}} \frac{\kappa_{Al}}{\kappa_{Ni}} \frac{I_{Ni}}{I_{Al}} = (0.7468)(1.491)(2.8) = 3.12$$

giving an apparent composition (wt%) $C_{Al} = 24.3$ and $C_{Ni} = 75.7$. Checking the validity of the thin-film approximation using the Tixier-Philibert criterion, one obtains $\chi \cdot \rho \cdot t \cong 0.02$ for the nickel K_α lines while $\chi \cdot \rho \cdot t \cong 0.9$ for the aluminum K_α line. Clearly, the Al K_α line violates the thin-film criterion and thus the effects of absorption must be included.

One begins the correction procedure by using Eqn. 4.22 to calculate the mass absorption coefficient of the NiAl alloy. From a suitable table of mass absorption coefficients (BRACEWELL and VEIGELE, 1970) one finds that the absorption coefficient for Al K_α x-rays in pure Al and Ni is respectively:

$$\left(\frac{\mu}{\rho}\right)_{Al}^{AlK_\alpha} \cong 410 \text{ cm}^2/\text{gm} \text{ and } \left(\frac{\mu}{\rho}\right)_{Ni}^{AlK_\alpha} \cong 4910 \text{ cm}^2/\text{gm}$$

while for the NiK_α line the values are

$$\left(\frac{\mu}{\rho}\right)_{Al}^{NiK_\alpha} \cong 63.7 \text{ cm}^2/\text{gm} \text{ and } \left(\frac{\mu}{\rho}\right)_{Ni}^{NiK_\alpha} \cong 60.6 \text{ cm}^2/\text{gm}$$

Using the compositions determined from the thin-film model, one obtains a first approximation to the true mass absorption coefficients for the NiAl alloy as:

$$\left(\frac{\mu}{\rho}\right)_{NiAl}^{AlK_\alpha} = (410)(0.243) + (4910)(0.757) = 3817$$

$$\left(\frac{\mu}{\rho}\right)_{NiAl}^{NiK_\alpha} = (63.7)(0.243) + (60.6)(0.757) = 61.4$$

Substitution of these values into Eqn. 4.21 yields a first order absorption correction of:

$$\frac{\delta_{Al}}{\delta_{Ni}} = 0.6486$$

and the resulting composition ratio using Eqn. 4.20 becomes

$$\frac{C_{Ni}}{C_{Al}} = \frac{\delta_{Al}\ \varepsilon_{Al}\ \kappa_{Al}}{\delta_{Ni}\ \varepsilon_{Ni}\ \kappa_{Ni}} \cdot \frac{I_{Ni}}{I_{Al}} = (0.6486)(0.7468)(1.491)(2.8) = 2.02$$

Thus after a first iteration the corrected compositions are:

$$C^{*}_{Al} = 33.1 \text{ and } C^{*}_{Ni} = 66.9$$

Using this result and proceeding through a second iteration the new values of mass absorption coefficients subsequently become:

$$\left(\frac{\mu}{\rho}\right)^{Alk_\alpha}_{NiAl} = (410)(0.331) + (4910)(0.669) = 3421$$

$$\left(\frac{\mu}{\rho}\right)^{Nik_\alpha}_{NiAl} = (6.37)(0.331) + (60.6)(0.669) = 61.6$$

This gives a new absorption correction term

$$\frac{\delta_{Al}}{\delta_{Ni}} = 0.6766$$

from which one obtains a calculated composition of

$$C^{**}_{Al} = 32.1 \text{ and } C^{**}_{Ni} = 67.8$$

A third iteration yields

$$C^{***}_{Al} = 32.2 \text{ and } C^{***}_{Ni} = 67.8$$

the ratio eventually converging toward $C_{Al} = 32.1$, $C_{Ni} = 67.9$ a value within 0.6% of the known specimen composition. The convergence in this example was particularly rapid and is a result of the initial thin film estimated composition being within about 7% of the actual composition.

The following results are obtained using the correction schemes outlined by Goldstein in the previous chapter. Using Eqns. 3.9, 3.10 and 3.14, k_{NiAl} at 200 KV is 1.18. If no absorption correction is made,

$$\frac{C_{Ni}}{C_{Al}} = k_{NiAl}\ \frac{I_{Ni}}{I_{Al}} = (1.18)(2.8) = 3.30$$

giving an apparent composition (wt%) $C_{Al} = 23.3$ and $C_{Ni} = 76.7$. Since an absorption correction is necessary one uses Eqn. 3.19 where

$$\frac{C_{Ni}}{C_{Al}} = k_{NiAl} \left\{ \frac{I_{Ni} \left(\frac{\mu}{\rho}\right)^{Ni}}{I_{Al} \left(\frac{\mu}{\rho}\right)^{Al}} \right\} \cdot \left\{ \frac{1-\exp - \frac{\mu}{\rho}^{Al} \cdot \rho \cdot t \cdot \csc\alpha}{1-\exp - \frac{\mu}{\rho}^{Ni} \cdot \rho \cdot t \cdot \csc\alpha} \right\}$$

In this equation α = the effective take off angle = 45° and all $(\frac{\mu}{\rho})$ values refer to the specimen. Following the iteration method outlined above, C_{Al} = 35.5 wt% and C_{Ni} = 64.5 wt% after the first iteration and C_{Ni} = 34.0 wt%, C_{Ni} = 66.0 wt% after the third iteration. The convergence is rapid and yields an Al value within 7% relative of the actual specimen composition (31.5 wt%). Such an error in a correction or relative composition shift of almost 50% may be acceptable, since other errors may be of comparable magnitude. For example, if the measured foil thickness is in error by ± 10%, the calculated Al composition will vary by more than ± 1 wt%.

The application of an absorption correction which results in compositions shifts of > 10% should be used with a great deal of caution. Specimen thicknesses sufficient to result in corrections this large will undoubtably have substantial beam broadening effects which can invalidate the geometry used in the formulation of the absorption correction. Furthermore, since the fluorescence correction is directly related to the magnitude of absorbed x-ray flux, working in specimen thickness with absorption corrections of < 10%, for the most part, insures that this correction will be small and can usually be neglected.

4.8 STANDARDLESS ANALYSIS IN COMPLEX SYSTEMS

In this section, the application of x-ray microanalysis to the quantitative interpretation of x-ray intensity measurements in complex multicomponent systems is considered. The term complex, in this context, is used to designate any analysis in which the investigator must pay close attention to the specific details of the experimental conditions or data reduction scheme used (beyond those general considerations discussed previously) to obtain accurate quantitative results. Three specific cases will be discussed below: 1. analysis of totally buried peaks; 2. procedures for accurate composition measurements of precipitates and 3. experimental techniques for analysis of radioactive specimens.

Analysis of Totally Buried Peaks

Due to the relatively poor resolution of solid state Si(Li) x-ray detectors, peak overlaps in multicomponent systems are a frequently observed phenomenon. This raises the question; how does one perform quantitative analysis when a peak is totally obscured by neighboring lines?

A particularly relevant example of this problem is the detection of low manganese concentrations in 316 stainless steels. In this situation the Mn K_α line (5.89 keV) is totally overlapped by the Cr K_β line (5.95 keV) while the Mn K_β peak (6.49 keV) is similarly buried under the Fe K_α line (6.50 keV). Fortunately, there is a solution to this apparent dilemma.

The answer is derived from the physics of the x-ray emission process, the relative intensities of all the characteristic x-ray lines from a particular shell are a constant for each element in the periodic table. This constant is, however, a function of atomic number. Typical values for the K_β/K_α ratio are in the range 0.1-0.25, while L shell values are more complex due to the multiplicity of observable emission lines. This variation is related to the intrinsic transition probabilities with a given subshell (DYSON, 1973); however, experimental factors such as self-absorption, detector efficiency, and the mode of excitation also influence the resulting values. Assuming one can obtain accurate values for the appropriate emission lines and the operating conditions employed, then the relative intensity relationships can be used to extract by difference (or deconvolution) the intensity of totally obscurred peaks.

Returning to the specific example of Mn analysis, Fig. 4.15 illustrates the detection of Mn using the relative intensity relationship between Cr K_α and K_β lines. Figure 4.16 (a) is an expanded region of the x-ray emission spectrum from a Fe-13Cr-40Ni specimen around the chromium K-shell lines. Experimental measurements from this specimen yield the following values for Cr, Fe, and Ni K_β/K_α ratios: Cr=0.137±0.001, Fe-0.148±0.001, Ni-0.149±0.001.

Figure 4.16. Illustration of Cr K_β - Mn K_α complete overlap situations (see text for details) (a) 0% Mn; (b) 1.8% Mn and (c) 8.9% Mn.

Figures 4.16 (b) and (c) show the magnitude of the resulting changes in CrK_β-MnK_α overlap peak which are observed during measurements of Mn rich inclusions in an inhomogeneous austenitic steel. Using the values for Cr K_β/K_α of 0.137 one obtains the local managanese compositions of 1.8 and 8.9 wt% for Figs. 4.16 (b) and (c) respectively. Although this example has dealt specifically with analysis of Mn in steel the technique is clearly applicable to similar overlap problems in any system, assuming of course that accurate measurements of the relative intensity ratios of the respective lines are available.

Quantitative Analysis of Precipitate Phases

Quantitative x-ray microanalysis of second phase precipitation in multicomponent systems is a nontrivial endeavor. Upon observing the presence of second phase regions within the microstructure of a specimen an investigator may attempt to perform analysis using the following procedure: 1. select an approriate imaging mode and probe size; 2. orient

ORNL-PHOTO 1668-79

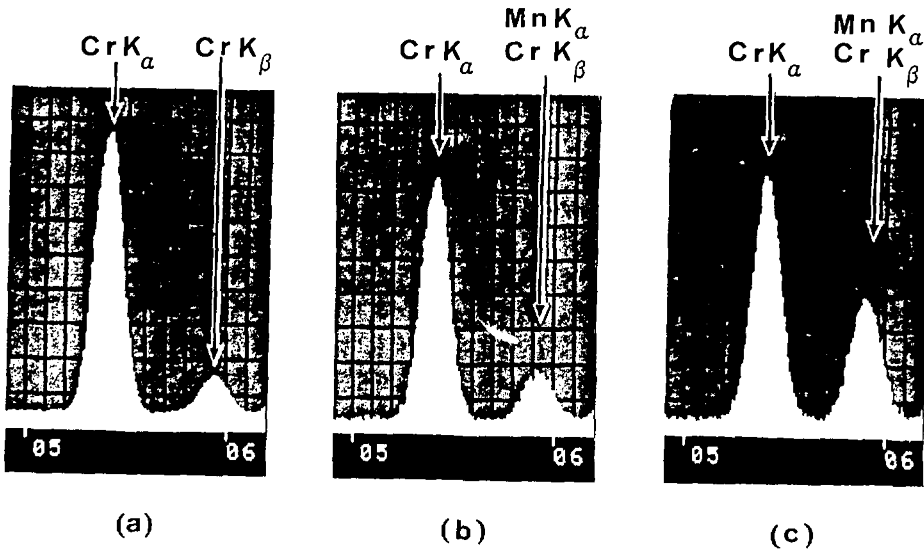

Figure 4.16. Illustration of Cr K_β - Mn K_α complete overlap situations (see text for details) (a) 0% Mn; (b) 1.8% Mn and (c) 8.9% Mn.

the specimen to avoid anamolous x-ray generation effects; 3. measure the characteristic x-ray spectrum from a second phase region in a thin region of the specimen; and 4. finally convert the relative intensity measurements into composition values using the thin-film equations.

The correct interpretation of the results obtained during such an experiment will depend greatly on: 1. the specific information desired by the analyst; 2. the relative amount of the second phase with respect to the host matrix in the excited volume; and 3. the relationship of the precipitate composition to that of the matrix phase.

The steps outlined above are adequate to provide qualitative or semi-quantitative information; however, quantitative interpretation can be difficult. The complications in this situation arise from the improper application of the thin-film formulation to analysis of the measured x-ray intensities. One should recall, here, that the thin-film equations have been derived assuming that the specimen composition is <u>homogeneous</u> over the analyzed volume. Put in another context, the application of the thin-film equations to heterogeneous regions effectively averages their composition over the excited volume. If the object of the experimental measurements is to accurately determine the composition of the precipitated phase, then one must effectively isolate it from the host matrix. This point is most clearly elucidated by reference to the following example.

Needle-like precipitates were observed to form in 316 stainless steel isothermally aged for 10,000 hours at 600 C (MAZIASZ, 1978). Subsequent crystallographic analysis identified these precipitates as having an fcc crystal structure and being consistent with the generic classification $M_{23}C_6$ (space group Fm3m, a ≅ 1.06 nm). In order to aid in the understanding of this precipitation process and its effects, accurate determinations of the precipitate composition are required. The <u>apparent</u> composition of this $M_{23}C_6$ phase measured under a systematic set of experimental configurations together with the composition of the aged 316 stainless steel matrix are documented in Table 4.7. The specific examples presented here were chosen to illustrate the potential for systematic errors which may occur during such an analysis.

The matrix composition reported in column 4 of this table was obtained by analyzing a region of the specimen < 200 nm thick approximately equidistant from all surrounding precipitates (the average inter-precipitate spacing was ∿ 500 nm). Column 3 presents the apparent composition observed when a STEM electron probe ∿ 10 nm in diameter (at 120 keV) was focussed on a $M_{23}C_6$ precipitate particle confined within the specimen matrix as shown in Fig. 4.17 (a). Here the precipitate thickness was ∿ 80 nm while the total thickness of the excited volume was on the order of 200 nm. Although the apparent composition is clearly different from matrix, this configuration for analysis is obviously far from optimum. A combination of beam broadening effects as well as the relative precipitate/matrix volume ratio will result in the partial detection of the matrix composition.

Figure 4.17. Needle-like $M_{23}C_6$ Precipitates in 316 Stainless Steel. (a) Embedded in Matrix; (b) Suspended from Edge of Specimen; (c) Extracted from Matrix.

With a sufficient amount of diligence on the part of the analyst it is usually possible to produce good quality TEM specimens in which the precipitates are partially isolated from the matrix by being suspended out from the foil edge [Fig. 4.17(b)]. Such a configuration improves the relative precipitate/matrix volume ratio and the measured compositions in this case (column 2, Table 4.7) are more representative of the second phase. However, a thin-shell of matrix material may still encapsulate the precipitate. In addition, material in the matrix nearby may be excited by electron scattered by the precipitate and by the contaminant. Thus, the analysis may be still only semi-quantitative. Note that the precipitate shown in Fig. 4.17(b) is clearly also surrounded by a substantial contamination layer produced by prolonged observation in a conventional TEM of relative poor vacuum. Thus, the anamolously high silicon content indicated can be ascribed to the presence of contamination prior to x-ray analysis in the AEM.

The most reliable measurements of the composition are obtained when the precipitate phase is extracted onto a thin carbon replica film using an electrochemical etching process [Fig. 4.17(c)]. The compositions measured here (column 1, Table 4.7) will most closely indicate the actual composition of the three measurements presented.

It is possible, of course, to propose a correction scheme in which one measures the relative volumes of the excited precipitate and matrix regions and then back-calculates the precipitate composition when the second phase is embedded within a matrix. However, not only does this require one to perform the difficult measurement of excited volume but it also requires a prior knowledge of the local matrix composition. Since the most significant precipitation phenomena result in the formation of composition gradients around second phase regions such a correction scheme may be more difficult than the experimental technique of extraction.

ORNL-PHOTO 1670-79

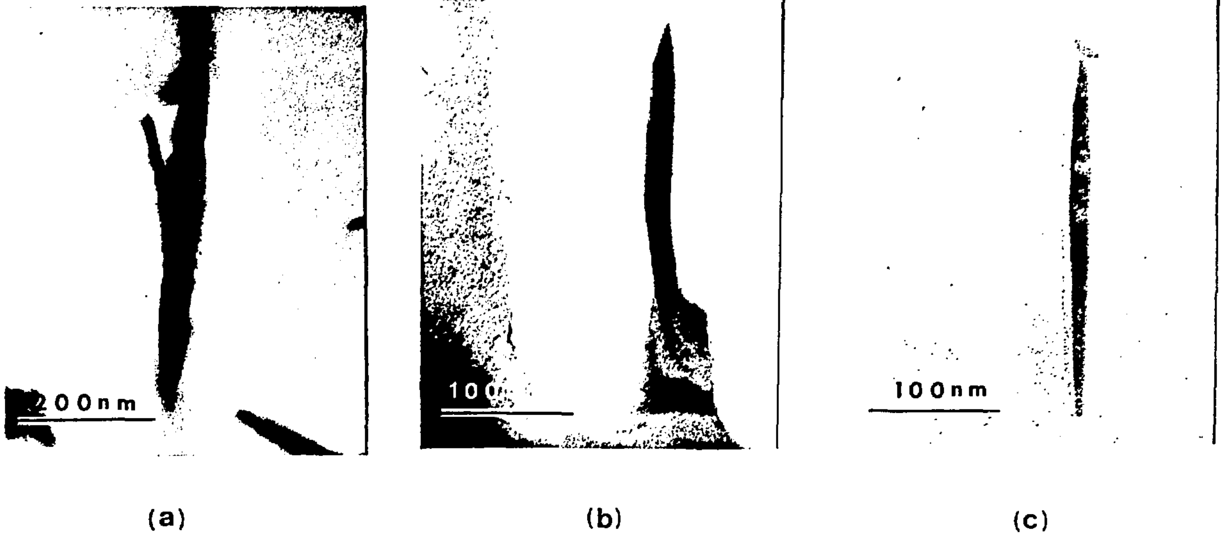

Figure 4.17. Needle-like $M_{23}C_6$ Precipitates in 316 Stainless Steel. (a) Embedded in Matrix; (b) Suspended from Edge of Specimen; (c) Extracted from Matrix.

Table 4.7

Analysis of $M_{23}C_6$ type precipitate in 316 stainless steel

Element	Composition (wt%) (1) Extracted Precipitate	(2) Suspended Precipitate	(3) Embedded Precipitate	(4) Matrix
Si	<.05	2.3*	1.1	1.3
Mo	16.7	14.2	8.7	3.9
Cr	65.9	58.2	30.9	18.4
Mn	<.05	0.2	1.47	1.5
Fe	14.6	21.6	47.9	62.3
Ni	2.8	3.6	10.0	12.6

*Increased silicon content probably due to presence of heavy contamination layer surrounding precipitate. (See figure 4.17b)

Table 4.8

Element	Apparent Matrix Composition (X-ray Microanalysis)	Bulk Analysis Prior to Irradiation (Wet Chemistry)
Si	2.4*	0.4
Mo	2.3	2.5
Ti	n.d**	0.25
Cr	18.5	17.0
Mn	n.d**	0.5
Fe	66.4	67.6
Ni	10.4	12.0
P,S,C	n.d**	0.08

*Specimen contamination due to prolonged observation in a conventional TEM will influence this measurement.

**No detectable peaks present above background after subtracting of in-hole signal.

Procedures for Analysis of Radioactive Specimens

The final topic considered within this chapter concerns the application of quantitative microanalysis to materials which have been introduced into reactor environments. The observation and characterization of the microstructure resulting from phase transformations produced during irradiation plays an extremely crucial role in understanding the materials subsequent macroscopic properties. Without such information one cannot logically proceed in a systematic development of candidate alloys for the various nuclear energy applications.

After a material has been subjected to a rector environment it generally becomes radioactive, which results in the specimen spontaneously emitting characteristic and continuum radiation to a varying degree. During microanalysis, this radiation will be detected simultaneously with any electron generated x-ray signal. If the specimen is sufficiently active $\gtrsim$ 10 μC the intensity of this intrinsic radioactive emission may dominate the electron excited x-ray signal. In fact, due to the large collection solid angle and short specimen-detector distances the intensity of the intrinsic emission can completely incapacitate the signal processing chain of the detector/multichannel analyzer system due to count rate limitations. The solution to this predicament is obvious but not necessarily simple - namely reduce the intensity of the radioactive emissions bombarding the Si(Li) detector. This is best accomplished using complementary approaches.

First procedure is for the investigator to reduce the excess mass of material present in the specimen, particularly that surrounding the rim of the TEM disc. The majority of the intrinsic emission comes directly from bulk regions at the periphery of the specimen. Since remote handling of these specimens is sometimes necessary during sample preparation one can only reduce the specimen size to a certain point. After this, one must resort to collimation of the x-ray detector system. The use of high atomic number collimators is particularly relevant here since the energy spectrum of the irradiated specimen may extend into the MeV range. Furthermore, most solid state Si(Li) are enclosed within relatively thin stainless steel detector heads, and it therefore may be necessary to wrap lead foil around the immediate vicinity of the detecting crystal to increase the shielding in this area. The specific amount of collimation required will obviously depend on the activity of the specimen being studied. Hopefully, one can by judiciously adjusting the collection solid angle achieve a condition in which intrinsic radioactive signal allows the analyst to measure in a realistic time frame a characteristic electron induced x-ray spectrum. An example of such an analysis is given below.

A specimen of titanium modified 316 stainless steel was irradiated in the High Flux Isotope Reactor (HFIR) at ORNL at 600°C to a neutron fluence producing the following conditions: 30 dpa (displacements per atom) and 1850 atomic ppm He. The specimen, after thinning into a 3 mm diameter TEM self-supporting disc had an activity of ~ 1000 μC and produced a radiation exposure level at contact of ~ 0.5 R/hr. These

radiations levels were sufficiently high that x-ray analysis in an AEM optimized for conventional x-ray work was completely prohibited. By constructing a suitable lead collimator adding lead shielding around the outside of Si(Li) detector, adjusting the collection solid angle to ∿ 5 x 10^{-4} sr and reducing the detector preamplifier time constant to 2 μsec it was possible to attempt microanalysis of this specimen. After these modification, the detector deadtime correction in the absence of an electron beam (i.e., the source turned off) was still ∿ 40%. Figure 4.18(a) shows the resulting beam-off spectrum recorded under these conditions, the characteristic Mn and Cr lines visible resulting from the nuclear decay process within the specimen (FARRELL, BENTLEY, and BRASKI, 1977; ENGE, 1966). The corresponding x-ray spectrum recorded with the electron probe (E = 120 keV) exciting a thin (< 200 nm) region of the matrix of the specimen is shown in Fig. 4.18(b). Although the electron

Figure 4.18. EDS Spectrum from Radioactive Ti-Modified 316 SS TEM Specimen. (a) Intrinsic Emission from Specimen; (b) Intrinsic Emmision + Electron Excited X-Rays

generated spectrum is clearly dominated by the intrinsic radioactive emission, one can still attempt a semi-quantitative analysis of the matrix composition by subtracting the resulting "in-hole" spectrum (i.e., spectrum produced by the combined effects of spontaneous emission and uncollimated fluorescence) from the total spectrum recorded during electron excitation of the matrix. The results of such an analysis are given in Table 4.8. Clearly, if the analyst desires more accurate results it will be necessary to reduce the intensity of the intrinsic emission to much lower levels than encountered here. This can be accomplished by altering the specimen preparation technique to reduce the excess sample mass surrounding the electron transparent zone. For example, the use of the window technique (HIRSCH et al, 1977) instead of the jet polishing method will substantially decrease the needless mass of bulk material surrounding the thin region of interest.

ORNL-PHOTO 1669-79

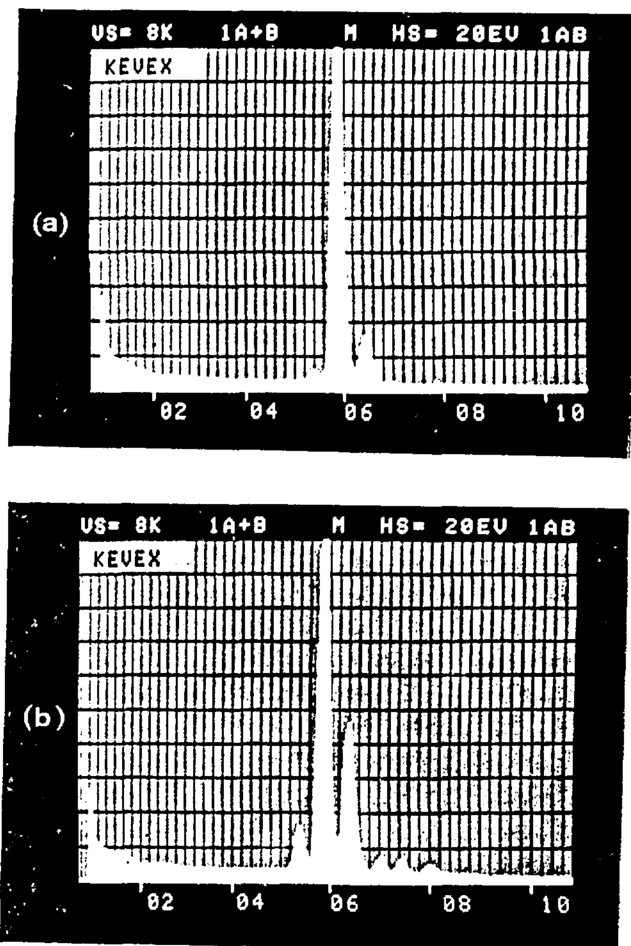

Figure 4.18. EDS Spectrum from Radioactive Ti-Modified 316 SS TEM Specimen. (a) Intrinsic Emission from Specimen; (b) Intrinsic Emmision + Electron Excited X-Rays

SUMMARY

There are a wide variety of instrumental problems which are present to some degree in all AEM instruments. The nature and magnitude of these artifacts can in some instances preclude the simple quantitative interpretation of the recorded x-ray emission spectrum using a thin-film electron excitation model; however, by judicious modifications to the instrument these complications can be effectively eliminated. The specific operating conditions of the microscope necessarily vary from one analysis to another depending on the type of specimen and experiment being performed. In general, however, the overall performance of the AEM system during x-ray analysis is optimized using the highest attainable incident electron energy; selecting the maximum probe diameter and probe current consistent with experimental limitations; and positioning the x-ray detector ina geometry such that it records information from the electron entrance surface of the specimen.

The application of standardless analysis to quantitative composition measurements from areas of a specimen which can be considered to be locally homogeneous is a relatively straightforward process. The accurate analysis of heterogeneous regions in complex alloy systems is on the other hand a more difficult proposal, due in part to the fact that one may not be able to uniquely separate the relative contribution to the measured x-ray spectrum from the different phases in the analyzed volume. Thus, the seemingly simple task of determining precipitate compositions in a thin-foil specimen can become a non-trival exercise if approached incorrectly.

ACKNOWLEDGMENTS

The author would like to acknowledge invaluable discussions and contributions to the work from the following scientists: J. Bentley, P. J. Maziasz, E. A. Kenik, R. W. Carpenter, J. B. Woodhouse, I. ~. Ward, and H. L. Fraser; and also to P. A. White, C. McKamey and M. Inman for their assistance in the preparation of this text. This work was supported by the E. P. Wigner Fellowship at ORNL.

REFERENCES

Arthurs, A. M. and Moiseiwitch, B. L., Proc. Roy. Soc. A247, 550 (1958).

Bentley, J., Zaluzec, N. J., Kenik, E. A., Carpenter, R.W., SEM/1979/ Washington, D.C., ed. O. Johari, Chicago Press (1979).

Bentley, J., and Kenik, E. A., Scripta Met., 11, 261-263 (1977).

Bentley, J. and Kenik, E. A., Oak Ridge Natinoal Laboratory, unpublished research, (1979). Available as ORNL TM/6857

Bracewell, B. L.,and Veigle, W. J., Developments in Applied Spectroscopy, 9, ed. A. Perkins, Plenum Press (1971).

Burhop, E. H. S., J. Phys. Radium, 16, 625 (1955).

Burhop, E. H. S., Proc. Cam. Phil. Soc., 36, 43 (1940).

Carpenter, R. W., Bentley, J., SEM/1979/ ed. O. Johari, pub. Chicago Press, Washington, D.C. (1979).

Clarke, D. R., SEM/1978/ 1 ed. O. Johari, pub. Chicago Press, Los Angeles (1978).

Cliff, G., Nasir, M. J., Lorimer, G. W., and Ridley, N., 9th Int. Con. on Electron Microscopy, ed., J. M. Sturgess, pub. Microscopical Society of Canada, Toronto (1978), 540-541.

Colby, J., Advances in X-Ray Analysis, 11, 287 (1968) (Plenum Press).

Dyson, N. A., X-Rays in Atomic and Nuclear Physics, Longman Group, Ltd., London (1973).

Duncumb, P., Phil. Mag., 7 (84), 2101 (1962).

Enge, H., Introduction to Nuclear Physics, Academic Press (1966).

Farrell, K., Bentely, J., and Braski, D., Scripta Met., 11, 243 (1977).

Fink, R. W., Jopson, R. C., Mark, H., and Swift, C. D., Rev. Mod. Phys., 39, 125 (1967).

Fiori, C. and Joy, D. C., National Institute of Health, Bethesda, Md., private communication (1979).

Fiori, C., Newbury, D., SEM/1978/1 ed. O. Johari, pub. Chicago Press, Los Angeles, 401 (1978).

Fraser, H. L., University of Illinois, Urbana, Illinois, private communication (1979).

Fraser, H. L. and Woodhouse, J. B., Electron Microscopy: Proc. of 2nd Workshop, Cornell University, Ithaca, NY, 191 (1978).

Geiss, R. H. and Huang, T. C., X-Ray Spectr., 4 (1975), 196-201.

Goldstein, J. I., Costley, J. L., Lorimer, G. W., and Reed, S. J. B., SEM 1, 315 (1977).

Goldstein, J. I. and Williams, D. B., SEM/1978/I, ed., O. Johari, pub. SEM Inc., AMF O'Hare, IL, 427-434 (1978).

Goldstein, J. I. and Williams, D. B., SEM/1977/1, ed., O. Johari, pub. Chicago Press, IIT Research Institute, Chicago, IL, 651-662 (1977).

Hall, C. R., Proc. Roy. Soc., A295, 140 (1966).

Hashimoto, H., Howie, A.,and Whelan, M., Proc. Roy. Soc., A269, 80 (1962).

Headley, T. J. and Hren, J. J., Sources of Background X-Radiation in AEM, ibid., 504-505.

Heinrich, K. F. J., Proc. 11th Conf. Mas (1976), p. 29.

Hirsch, P., Howie, A., Nicholson, R., Pashley, D., Whelan, M., Electron Microscopy of Thin Crystals, Krieger Pub. Co., New York, 1977.

Hink, W. and Ziegler, A., Z. Physik, 226, 222 (1969).

Hutchings, R., Loretto, M. H., Jones, L. P., Smallman, R. E., Analytical Electron Microscopy, 2nd Workshop, Cornell University, Ithaca, New York, 166 (1978).

Hren, J. J., Ong, P. A., Johnson, P.D., and Jenkins, E. J., 34th Proc. EMSE, ed., Bailey, G. W., pub. Claitor's, Baton Rouge, 1976, 418-419.

Johnson, P. F., Bates, S. R., and Hren, J. J., 9th Int. Conf. on Electron Microscopy, ed., Sturgess, pub. Microscopical Society of Canada, Toronto, 1978, 502503.

Joy, D. C.,and Maher, D. M., Analytical Electron Microscopy: Report of a Specialist Workshop, Cornell University (August, 1976), 111113. Materials Science Center, Clark Hall, Cornell University, Ithaca, N.Y. 14850.

Joy, D. C., Maher, D. M., SEM/1977, ed. O. Johari IITRI, Chicago, IL, 325 (1977).

Kenik, E. A., Bentley, J., 35th Ann. Proc. of EMSA, ed., G. W. Bailey, pug. Claitor's, Baton Roughe (1977), 328329.

Lorimer, G. W., Cliff, G., and Clark, J. N., pp. 153159, Developments in Electron Microscopy and Analysis, Academic Press, London, 1976.

Kirkpatrick, P. and Wiedmann, L., Phys. Rev. 67, 321 (1945).

Kirkpatrick, P., and Baez, A. V., Phys. Rev. 71, 521 (1947).

Liljesvan, B., and Roomans, G. M., Ultramicroscopy 2 (1976) 105-107

Lorimer, G. W., Cliff, G., and Clark, J. N., pp. 153-159, Developments in Electron Microscopy and Analysis, Academic Press, London, 1976.

Maziasz, P. J., Proc. of Symposium Metal Physics of Stainless Steel, TRMKAIME Meeting, Denver, 1978.

Morris, P. L., Davis, N. C., and Treverton, J. A., Developments in Electron Microscopy 1977: Proc. of EMAS, ed., D. L. Misell, Pub. Inst. of Phys., Briston, England, 2377380.

Mott, N., and Massey, H., Theory of Atomic Collisions, Oxford Press, London, 1949.

Oppolzer, H., and Knauer, U., SEM/1979, Washington, D.C., ed., O. Johari, pub. Chicago Press.

Perlman, H. S., Proc. Phys. Soc. (London), 76, 623 (1960).

Philibert, J.,and Tixier, R., (1968) B. J. A. P. 1, 685.

Pockman, L. R., Webster, D. L., Kirkpatrick, P., and Harworth, K., Phys; Rev. 71, 330 (1947).

Powell, C. J., Rev. Mod. Phys. 48, 33 (1976).

Reed;, S. J. B., The Electron Microprobe Analysis, Cambridge University Press (1976).

Robertson, B. W., Chapman, J.N., Nicholson, W. A. P., and Ferrier, R. P., 9th Int. Conf. on Electron Microscopy, ed., J. M. Sturgess, pub. Microscopical Society of Canada, Toronto (1978), 550-551.

Shuman, H., Somlyo, A. V., and Somlyo, A. P., Ultramicroscopy 1 (1976) 317-339.

Slivinsky, V. W., and Ebert, P. J., Phys. Rev. A 5, 1581 (1972).

Sommerfeld, A., Ann. d. Physik 11, 257 (1931).

Sturcken, E. F., SEM/1976/I, ed., O. Johari, pub. Chicago Press, IIT Research Institute, Chicago, IL, 247-256 (1976).

Sprys, J. W., Rev. Sci. Instr. 46 [6] (1975) 773-774.

Wentzel, G. Z., Phys. 43, 514 (1927).

Woldseth, R., X-ray Energy Spectrometry, pub. Kevex Corp., (1973), Burlingame, CA.

Worthington, C. R., and Tomlin, S. G., Proc. Phy. Soc. (London), 69, 401 (1956).

Zaluzec, N. J., Ninth Int. Cong. on Electron Microscopy, ed., J.M. Sturgess; pub. Microscopical Society of Canada, Toronto, 1978, Vol. 1, 548-549.

Zaluzec, N. J., Kenik, E. A., and Bentley, J., Analytical Electron Microscopy; Proc. of 2nd Workshop // at Cornell University, July 1978, 179.

Zaluzec, N. J., and Fraser, H. L., 8th Int. Conf. on X-ray Optics and Microanalysis, Boston, 1977, ed., Beaman, Ogilivie, Wittry, pub. Science Press, Princeton, N.Y. (in press).

Zaluzec, N. J., and Fraser, H. L., Analytical Electron Microscopy: Report of a Specialist Workshop, Cornell University (August 1976), 118-120. Materials Science Center, Clark Hall, Cornell University, Ithaca, N. Y. 14850.

Zaluzec, N. J., and Fraser, H. L., 34th Ann. Proc. of EMSA, ed., G. W. Bailey, pub. Claitor's, Baton Rouge (1976), 420-421.

Zaluzec, N. J. and Fraser, H. L., Analytical Electron Microscopy; Proc. of the 2nd Workshop, Cornell University, Ithaca, N.J., July 1978, 122.

Zaluzec, N. J., And Fraser, H. L., Phys. E. 9 (1976) 1051-1052).

Zaluzec, N. J., An Analytical Electron Microscopy Study of the Omega Transformation in a Zirconium-Niobium Alloy Phase, Ph.D. Thesis, University of Illinois, 1978; also published as Oak Ridge National Laboratory Report ORNL/TM6705. Copies available from NTIS, U. S. Department of Commerce, Springfield, VA 22161.